Asian and trans-Pacific dust: a multi-model and multi-remote sensing observation analysis

Article

Accepted Version

Asian and trans-Pacific Dust: A multi-model and multi-remote sensing observation analysis

Dongchul Kim[1,2], Mian Chin[2], Hongbin Yu[2], Xiaohua Pan[2,3], Huisheng Bian[2,4], Qian Tan[5,6], Ralph A. Kahn[2], Kostas Tsigaridis[7,8], Susanne E. Bauer[7,8], Toshihiko Takemura[9], Luca Pozzoli[10], Nicolas Bellouin[11], and Michael Schulz[12]

[1]Universities Space Research Association, Columbia, Maryland, USA
[2]Earth Sciences Division, NASA Goddard Space Flight Center, Greenbelt, Maryland, USA
[3]Earth System Sciences Interdisciplinary Center, University of Maryland, College Park, Maryland, USA
[4]JCET/UMBC, Baltimore County, Baltimore, Maryland, USA
[5]Bay Area Environmental Research Institute, Moffett Field, California, USA
[6]NASA Ames Research Center, Moffett Field, California, USA
[7]NASA Goddard Institute for Space Studies, New York, New York, USA
[8]Center for Climate Systems Research, Columbia University, New York, New York, USA
[9]Research Institute for Applied Mechanics, Kyushu University, Fukuoka, Japan
[10]European Commission - Joint Research Center, Ispra, Italy
[11]Department of Meteorology, University of Reading, Reading, UK
[12]Norwegian Meteorological Institute, Oslo, Norway

Corresponding author: Dongchul Kim (dongchul.kim@nasa.gov)

Key points:

- Dust and total aerosol over Asia and the North Pacific Ocean are evaluated using observations and models.
- Satellites estimate that a 35-70 % decrease of DOD from the west Pacific to the east Pacific.
- Diversity of DOD is mostly driven by the diversity of the dust source followed by residence time and mass extinction efficiency.

Abstract

Dust is one of the dominant aerosol types over Asia and the North Pacific Ocean, but quantitative estimation of dust distribution and its contribution to the total regional aerosol load from observations is challenging due to the presence of significant anthropogenic and natural aerosols and the frequent influence of clouds over the region. This study presents the dust aerosol distributions over Asia and the North Pacific using simulations from five global models that participated in the AeroCom phase II model experiments, and from multiple satellite remote-sensing and ground-based measurements of total aerosol optical depth (AOD) and dust optical depth (DOD). We examine various aspects of aerosol and dust presence in our study domain: (1) the horizontal distribution, (2) the longitudinal gradient during trans-Pacific transport, (3) seasonal variations, (4) vertical profiles, and (5) model-simulated dust life cycles. This study reveals that the diversity of DOD is mostly driven by the diversity of the dust source followed by residence time and mass extinction efficiency.

1. Introduction

Dust aerosol can impact the Earth's weather, climate, and eco-systems by interacting with solar and terrestrial radiation, altering cloud amount and radiative properties, fertilizing land and ocean, and modulating carbon uptake (Haywood et al., 2003; Jickells et al., 2005; Forster et al., 2007; Evan et al., 2008; Kim et al., 2010; Maher et al., 2010; Creamean et al., 2013; Yu et al., 2015a; Song et al., 2018). The majority of global dust sources are from arid surfaces such as North Africa, the Middle East, and

parts of Asia, and to a lesser extent Australia and Patagonia (e.g., Tegan et al., 2002; Prospero et al., 2002; Huneeus et al., 2011; Ginoux et al., 2012).

Although dust emission from Asia is estimated as only 25~35% of that from North Africa (Chin et al., 2007; Su and Toon, 2011; Ginoux et al., 2012), it is a dominant source of dust not only over the land areas of Asia. Asian dust is also significant over the North Pacific Ocean, western North America, and the Arctic (e.g., Chin et al., 2007) via long-range transport, playing a key role in the climate and eco-system in these regions (Uno et al., 2009; Shao et al., 2011; Yu et al., 2012). Observation-based estimates of dust amount based on multiple years of satellite AOD data from the Moderate Resolution Imaging Spectro-radiometer (MODIS) suggest that about 140 Tg (1 Tg = 10^6 tons) of dust are exported from East Asia; among which 56 Tg (40%) reach the west coast of North America, and the remaining 84 Tg are deposited in the North Pacific and/or are transported to the Arctic (Yu et al., 2012). Dust is more efficiently transported across the North Pacific Ocean (40%) than other continental aerosols (25%) (Yu et al., 2008) due to the higher elevation of dust layers (Yu et al., 2010, 2012). The satellite-based estimate of trans-Pacific dust transport and deposition differs significantly from those estimated from in-situ measurements and simulated by models, as summarized in Yu et al. (2013).

On the other hand, previous modeling studies of dust outflow from Asia and deposition to the North Pacific have shown different results. A study with the Northern Aerosol Regional Climate Model estimated that out of 120 Tg of dust (< 41 μm in diameter) emitted from Asia in Springtime, 31 Tg (26%) is exported from Asia to the Pacific Ocean and only 4 Tg (13%) of the exported dust reaches North America (Zhao et al., 2006). An inter-model comparison study with eight regional dust emission/transport

models demonstrated that participating dust models differ by a wide range over Asia, from emission to surface concentration, horizontal distribution, and vertical profiles during long-range transport (Uno et al., 2006). They suggested that measurements of dust fluxes and accurate, up-to-date land-use information are crucial to achieve more realistic simulations over these regions. Dust simulated from global models have also been extensively compared in the past AeroCom studies (Kinne et al., 2006; Huneeus et al., 2011; Koffi et al., 2012, 2016; Kim et al., 2014), but none of them specifically devoted to assessing model performance in the Asian-Pacific region, partially due to the lack of reliable data over this region. For example, Huneeus et al. (2011) pointed out that a specific Asian dust data set is needed to evaluate the global dust models, and suggested that one way to assess the performance of global dust models over Asia would be to compare measurements of coarse-mode AOD against modeled ones. However, extracting dust data from satellite observations in the Asian-Pacific region is challenging because of the frequent cloud occurrence in the North Pacific and the large amount of pollution aerosol over the Asian continent. Wu et al. (2019) showed that different dust retrieval algorithms based on the CALIOP observations yield significant differences in the dust vertical distribution, which complicates the evaluation of model simulations.

With the recent development of methods to derive satellite-based dust vertical profiles and transport flux estimates based on the CALIOP and MODIS data (Ginoux et al., 2012; Yu et al., 2015a, b; Yu et al., 2019a, 2019b), we present in this paper an evaluation of multiple, global model dust simulations in the Asian-Pacific region from the AeroCom Phase II (AeroCom II) Hindcast model experiment with multiple satellite observations. We also examine several key physical and optical model parameters in

order to explain discrepancies between observations and models, and among the models. We use an approach similar to our previous study (Kim et al., 2014), that evaluated AeroCom II model-simulated dust with updated satellite observations in the African-North Atlantic region, and addressed the key processes causing model diversity and deficiency.

In section 2, we briefly describe the AeroCom II Hindcast model simulations and the satellite- and ground-based remote-sensing data. In section 3, we compare the observed and modeled total aerosol and dust aerosol optical depths, including their longitudinal gradients and vertical distributions. In section 4, we investigate details of the dust life cycle in the models, and we compare results from the present study with those of North Africa. Discussion is presented in section 5, followed by a summary in section 6.

2. Models and data

2.1 AeroCom models

AeroCom is an internationally coordinated effort to advance the understanding of atmospheric aerosols and to document and diagnose differences between models and between models and observations (http://aerocom.met.no). The AeroCom II Hindcast experiments produced multi-year simulations from 1980 to 2007, but models cover different simulation lengths. Following Kim et al. (2014), we use the five AeroCom models that provided dust simulations and diagnostics over the time period 2000-2005. The model setup and configurations are highly model-dependent, for example, with horizontal resolution from 1.1° in SPRINTARS to 2.8° in ECHAM5 (Table 1). Vertical coordinates range from 30 layers in GOCARTv4 (hereafter GOCART) to 56 in

131 SPRINTARS. The meteorology fields that drive dust emissions and transport are taken
132 from three reanalysis products, namely NCEP (used by SPRINTARS and GISS-E2-
133 OMA, formerly known as GISS-modelE and hereafter as GISS), ECMWF (used by
134 HadGEM2 and ECHAM5-HAMMOZ, hereafter ECHAM5), and GEOS4 (used by
135 GOCART). Some models use 10-m wind for dust mobilization parameterization
136 (GOCART, GISS, and SPRINTARS), whereas others use friction velocity (u^*)
137 (ECHAM5 and HadGEM2). Dust density values are similar among the models, ranging
138 from 2.5 to 2.65 g cm^{-3}. The range of dust size and the number of size groups are
139 different among models (Table 1). GOCART and SPRINTARS has the same size range
140 (0.1-10 μm in radius) but different size bins (5 and 6, respectively), GISS includes more
141 extended particle sizes (0.1-16 μm) with 5 size bins, and HadGEM2 covers a wider range
142 of dust particle sizes (0.03-31.6 μm) in 6 size bins. By contrast, ECHAM5 includes only
143 sub-micron particles, in 2 modes ranging from 0.05 to 0.5 μm. The differences in size
144 distribution affect total dust mass amount included in emission, transport, deposition
145 fluxes, mass loading, and overall lifetime, as well as the average mass extinction
146 efficiency that converts mass to light-extinction in different models.
147 Participating models commonly have two dry removal processes of 1)
148 gravitational settling as a function of aerosol particle size and air viscosity (Fuchs, 1964)
149 and 2) surface deposition as a function of surface type and meteorological conditions
150 (Wesely 1989). Wet scavenging removal in each model is empirically parameterized with
151 the precipitation rate and the scavenging coefficient; thus, a wide range of scavenging
152 coefficients are found among the models. Both GOCART and GISS have similar wet
153 scavenging parameterizations based on the previous work (Giorgi and Chameides 1986;

154 Balkanski et al., 1993), where Balkanski et al. (1993) adopted a 50% aerosol scavenging
155 efficiency in shallow convection and a 100% scavenging efficiency in deep convection.
156 SPRINTARS uses a size dependent collision efficiency with raindrops (Equation A6 in
157 Takemura et al., 2000); HadGEM2 uses a particle-size-dependent scavenging coefficient
158 (2×10^{-5} for <0.3 μm ~ 4×10^{-4} for >3.16 μm) (Table 1 in Woodward, 2001); ECHAM5 has
159 a scavenging parameter in the range of 0.1~0.9, depending on cloud type (stratiform or
160 convective cloud), or cloud status (liquid, mixed, or ice cloud), and mixing status (Table
161 3 in Stier et al., 2005).

162 Overall, dry and wet deposition efficiencies are highly empirical, and depend on
163 the vegetation type, surface conditions, atmospheric stability, particle sizes, and
164 meteorological fields. The model diversity in deposition processes is found from the
165 differences in the spatial distributions of LF and f_{WET} (Figure 10) between models. The
166 differences in size range also affect model diversity in many dust-associated fields,
167 including net emission amount, dry deposition, and DOD.

168 We compare several monthly mean fields from the model output with remote
169 sensing data or observation-derived quantities, namely the total aerosol optical depth
170 (AOD), dust aerosol optical depth (DOD), and the vertical extinction profiles of total and
171 dust aerosols (σ_{aer} and σ_{du}, respectively, in km^{-1}). Since the dust vertical extinction
172 profiles from the models were not available in the AeroCom archive, they are constructed
173 from the model-calculated dust mass concentrations and the mass extinction coefficient,
174 assuming dust does not take up water vapor, such that DOD does not depend on the
175 ambient relative humidity. The dust mass extinction coefficient is obtained by dividing
176 model calculated DOD with dust mass loading. In addition, model-calculated dust mass

177 loading (LOAD), emission (EMI), dry deposition (DRY), wet deposition (WET), and
178 total precipitation are used to assess possible causes of the inter-model diversity.
179 When comparing with satellite retrievals and AERONET observations that are
180 available only under clear-sky conditions, it is desirable to use the modeled AOD for
181 clear-sky as well. However, only the GISS model provides such output (other models just
182 provide all-sky results). A previous study showed that clear-sky AOD from the GISS
183 model is 30% lower than all-sky AOD over the North Africa-Northern Atlantic region
184 (Kim et al., 2014). In another estimate based on the GEOS-Chem model, clear-sky AOD
185 is 20% lower than all-sky AOD on global average (Yu et al., 2012). DOD is not sensitive
186 to differences between clear-sky and all-sky conditions due to the hydrophobic nature of
187 dust (Kim et al., 2014), although the different averaging times between all-sky and clear-
188 sky conditions are also expected to produce different AOD values. DOD in ECHAM5 is
189 approximated from the dust volume-weighted AOD of two internally mixed modes where
190 dust is present (Stier et al., 2005). The internal mixing of dust has the potential to cause
191 additional differences between ECHAM5 and other models in the inter-model
192 comparison. Although some models do not consider the chemistry on dust surfaces,
193 previous studies have estimated that the enhanced hygroscopicity of dust by
194 heterogeneous mixing can reduce the global dust burden on 17%~28% in GISS (Bauer
195 and Koch, 2005) and 5% in ECHAM5 (Pozzoli et al., 2008).
196
197 2.2 Remote sensing data
198 2.2.1. Vertical profiles

To evaluate the vertical distribution of dust, we use the aerosol and dust extinction profiles from CALIOP at 532 nm, following the method developed by Yu et al. (2015b). As CALIOP data are only available after June 2006, we use the monthly CALIOP data averaged from 2007 to 2011. The difference of time periods between CALIOP and model simulations may cause some vertical profile differences; however, its effect is not expected to be significant, as the climatological data is averaged over a large domain for a long time. Mean extinction profiles of total and dust aerosol are derived from version 4.10 CALIOP Level 2 aerosol profile data with a nominal along-track resolution of 5 km and vertical resolution of 30 m.

The first step is to collect quality-assured aerosol extinction profile data. Here, we use cloud-free nighttime CALIOP data to minimize interference from clouds and sun, and select extinction profiles with good retrieval quality, i.e., QC flag of 0, 1, 16, or 18, following recommendations by Winker et al. (2013). We then separate aerosol from clouds according to the cloud-aerosol-discrimination (CAD) scores, for which the aerosol scores are typically in the range of -100 to -20 (Winker et al., 2013; Tackett et al., 2018). However, in this study we choose a more stringent CAD-score range of -100 to -70 when selecting aerosol data (Yu et al., 2019a), which provides greater confidence in excluding possible cloud contamination. Compared to the relatively relaxed criteria of CAD between -100 and -20, the total aerosol sampling is reduced by up to 15% with our stricter criteria (Figure S1).

The dust fraction for backscatter in each profile is calculated using the CALIOP observed particulate depolarization ratio (dp), as coarse, non-spherical dust particles produce a depolarization signal. The maximum threshold value ($dp > 0.2$) and the dp of

non-dust particles is assumed to be 0.02 (Hayasaka et al., 2007, Tesche et al., 2009, and Yu et al., 2012, 2015b, 2019a). A constant lidar ratio value of 44 sr^{-1} (Omar et al., 2010; Young et al., 2018) is used to convert dust backscatter to dust extinction at 532 nm. We calculate the average vertical extinction profile using all the individual profiles during a month within the 2° in latitude × 5° in longitude grid. All averaged total and dust aerosol profiles are at 60-m vertical resolution.

Aerosol extinction is retrieved only where aerosol is detected by the CALIOP feature finder. However, in reality aerosol is present virtually everywhere throughout the troposphere, although aerosol concentration can be very low in pristine oceanic regions. When the aerosol signal is weak, below CALIOP detection limit, no feature is detected in the level 2 atmospheric sounding, and the sample is classified as "clear-air." Aerosol extinction is set to zero (km^{-1}) in the level 3 algorithm, whereas several studies have sought to characterize the optical depth of aerosol layers undetected by CALIOP (Tackett et al. (2018) and references therein). For data identified as "clear-air" in the present comparison, we adopt the approach used in generating the standard level-3 product (Tackett et al., 2018). However, this could cause a low bias in the averaged data because aerosols at low concentrations are missing, especially over the Pacific Ocean. This may also introduce a difference in the shape of aerosol profile because CALIOP tends to detect "clear-air" more often in free troposphere than in the atmospheric boundary layer. In addition to the level 3 algorithm method, we further average the vertical profiles, but excluding "clear-air" data from the averages, which we could expect to represent an upper bound on the profile data. The results are discussed in section 5.

245 2.2.2. AOD and DOD

246 The observational datasets used to evaluate the model simulations are listed in
247 Table 2. Seasonal and spatial distributions of AOD are taken from the Moderate
248 Resolution Imaging Spectroradiometer (MODIS) at 550 nm and the Multiangle Imaging
249 SpectroRadiometer (MISR, version V22) at 555 nm on board the EOS-Terra satellite.
250 The merged MODIS dataset used here is the Collection 6 version with combined retrieval
251 results from the Dark Target and Deep Blue algorithms (Levy et al., 2013). Whereas the
252 Dark Target algorithm provides observations over ocean, the Deep Blue algorithm
253 provides observations over bright land and desert scenes using the deep-blue wavelengths
254 (i.e., 0.41 and 0.47 μm).

255 MODIS AOD over ocean and fine-mode fraction (f) measurements have been
256 used to empirically separate dust (du) AOD from that of combustion aerosol (co) and
257 marine aerosol (ma) in a self-consistent way (Kaufman et al., 2005; Yu et al., 2009,
258 2019b). Given that $\tau = \tau_{ma} + \tau_{du} + \tau_{co}$ and $f = [f_{ma}\tau_{ma} + f_{du}\tau_{du} + f_{co}\tau_{co}]/\tau$, dust optical depth ($\tau_{du}$
259 or DOD) is derived from the MODIS Collection 6 data using representative values for
260 f_{ma}, f_{du}, f_{co}, and τ_{ma} (Yu et al., 2019b). Although large spatial and temporal variability of
261 f_{ma} is accounted for following a method in Yu et al. (2009), we assume constant values
262 for f_{du} and f_{co} because of lack of observational constraints. In this study, marine AOD is
263 parameterized as a function of surface wind speed derived from previous studies (Yu et
264 al., 2019b). A detailed description of the method, including uncertainty estimates and
265 assumptions, can be found in the literature (Yu et al., 2009 and 2019b). DOD over land is
266 also derived from MODIS Collection 6 data but with an approach different than ocean,
267 because MODIS fine-mode fraction retrieval over land is less reliable. Over land, DOD is

extracted from the MODIS Deep Blue (MDB) datasets, based on 1) the co-function of the continuous angstrom exponent values derived by Anderson et al. (2005), 2) single scattering albedo ω at 412 nm less than 1, and 3) a positive difference of ω between 412 and 670 nm ($\omega_{670} - \omega_{412} > 0$) (Ginoux et al., 2012; Pu and Ginoux, 2016).

Similar to our previous study of transatlantic dust (Kim et al., 2014; Guo et al., 2013), we use MISR AOD over land and ocean, and the non-spherical AOD over ocean, as a proxy for DOD (Kalashnikova and Kahn, 2006; Kahn et al., 2010). Non-spherical AOD is generally of higher quality over ocean for MISR, due to uncertainties in accounting for the brighter and more varying land surface (Kahn and Gaitley, 2015). However, the frequent interference by clouds, especially thin cirrus, contributes to the AOD and the non-spherical AOD uncertainties over the study region (Pierce et al., 2010). Note also that for both MODIS and MISR, sensitivity to the particle-property proxies used to identify the dust component diminishes when the total mid-visible AOD falls below about 0.15 or 0.2. The resulting uncertainty probably contributes significantly to the differences in MODIS and MISR DOD presented in the section 3 below, especially in the low-AOD areas over ocean.

CALIOP monthly AOD and DOD is calculated by vertically integrating the total and dust aerosol extinction coefficient profile at 532 nm, respectively, as described in the previous section.

We also use total AOD and coarse-mode AOD at 550 nm (Version 2, Level 1.5 and 2) from ground-based AErosol RObotic NETwork (AERONET) (Holben et al., 1998) sites located within the study domain to evaluate both satellite measurements and model simulations, although not all coarse-mode aerosols are dust, and some dust is in

291 the fine-mode. Twenty-nine AERONET sites were chosen, to allow enough geographical
292 coverage across the study region (see Table S1 for the latitude and longitude coordinates
293 of these sites). However, AERONET data are rather limited over the ocean in our study
294 domain and time period, as only two remote AERONET sites, in Midway and Hawaii,
295 are available in the northern Pacific, and the AERONET-coordinated Maritime Aerosol
296 Network (MAN, http://aeronet.gsfc.nasa.gov/new_web/man_data.html) data are not
297 available in the Pacific during the study period.

298 All the model-data comparisons are performed on a monthly, seasonal, or multi-
299 year average basis. This approach may introduce some differences between satellite data
300 and model results because of location and time mis-matches; however, given the large
301 amount of data in our expansive domain over a six-year time span, it should not affect
302 our statistics and conclusions, as shown in several previous evaluation studies (e.g., Chin
303 et al., 2007, 2014; Colarco et al., 2010; Randles et al., 2017). Also, additional caution is
304 needed when comparing remote-sensing-derived and modeled DOD and dust extinction
305 profiles, as the dust data from remote sensing are either dust proxies, or are obtained with
306 several assumptions, and are thus subject to large uncertainties.

307

308 3. Evaluation and comparisons of model simulations with observations

309 In this section, we evaluate the model results with satellite and ground-based
310 remote sensing data by comparing (i) the mean AOD and DOD in the study domain; (ii)
311 the longitudinal gradient of AOD and DOD from the dust source region in East Asia to
312 the downwind areas in the Pacific; (iii) the seasonal variations of AOD and DOD; and
313 (iv) the vertical profiles of aerosol and dust over land and ocean. The results are

314 summarized in Tables 3 and 4. A study domain (60°E~120°W; 10°N~70°N) was chosen
315 to cover dust source regions in Asia and the trans-Pacific transport route. We divide the
316 study area into land (60°E-140°E; 20°N-60°N) and ocean (140°E-140°W; 20°N-60°N)
317 regions and define six sub-domains for vertical profile analysis. Detailed domain
318 information is provided in Figure 1.
319
320 3.1 Mean AOD and DOD
321 Figure 2 shows a comparison between satellite observations and model
322 simulations of the 6-year mean total AOD averaged from 2000 to 2005, with AERONET
323 AODs at 29 sites superimposed using the same color scale. MODIS and MISR agree
324 within 15 % over the study domain (average AOD = 0.226 and 0.194, respectively), with
325 larger difference over land (0.274 and 0.209) than over ocean (0.177 and 0.179) (Table
326 3). These results reflect the known behavior of the MISR and MODIS products (e.g.,
327 Kahn et al., 2009). On the other hand, the CALIOP AOD is significantly lower than
328 MODIS (47 % lower over ocean and 21 % lower over land compared to MODIS), which
329 is also shown in previous studies (Redemann et al., 2012; Kim et al., 2013). There are a
330 few known factors that contribute to the uncertainty of CALIOP AOD over the study
331 domain, including the underestimation of aerosol extinction in the upper troposphere due
332 to the detection limit (Winker et al., 2013), and the narrow lidar swath that may miss
333 some episodic aerosol plumes (Yu et al., 2013).
334 The satellites and AERONET show high annual mean AOD (>0.4) over East
335 China and the Indo-Gangetic Plain, which are known to be highly polluted regions.
336 Models capture the geographical pattern of the AOD distribution from the satellites, i.e.,

337 the higher AOD over polluted regions, the decreasing gradient over ocean from west to
338 east, and northward shifting of the AOD plume center toward the eastern Pacific. Satellite
339 AOD better agrees with AERONET and gives better statistics, showing higher correlation
340 and lower bias than the models (Figure S2). The multi-year domain-averaged AOD from
341 the models differs within 50%, ranging from 0.16 (SPRINTARS) to 0.20 (GOCART)
342 (20%) over the entire domain, 0.18 (ECHAM5) to 0.25 (GOCART) (24%) over land, and
343 0.11 (SPRINTARS) to 0.19 (GISS) (42%) over ocean.
344 For dust, satellite-derived DOD is available from MODIS and CALIOP over both
345 land and ocean and MISR only over ocean (Figure 3). Both MODIS and CALIOP
346 products show substantial dust presence (DOD>0.2) over the land source regions of
347 Taklimakan desert, Thar desert, Gobi desert, and Loess Plateau, and the areas
348 immediately downwind. The MODIS and CALIOP DOD values (0.11 and 0.09,
349 respectively) over land are supported by the coarse-mode AOD (proxy for DOD) from
350 AERONET. Over ocean, all satellite data show transported DOD plumes over the
351 northwestern Pacific (i.e., east of 150°W; 30°N-50°N), but the magnitude from CALIOP
352 is much lower than MODIS and MISR. On average, DOD over ocean from CALIOP
353 (0.027) is 54% and 50% lower than that from MODIS (0.059) and MISR (0.054),
354 respectively. The average dust fractions of mid-visible AOD from MODIS and CALIOP
355 are about 36 and 42 % over land and 30 and 29 % over ocean, respectively.
356 Compared to the relatively small difference (~20%) of average AOD among
357 models (AOD = 0.16-0.20), the difference in average DOD is much larger – a factor of
358 10 in the domain-average (0.008-0.08). Over land, DOD from ECHAM5 (0.01) and
359 HadGEM2 (0.02) are significantly lower than satellites (0.09-0.11) and other models

360 (0.05-0.11). The underestimation of DOD in ECHAM5 and HadGEM2 is attributed to
361 lower emissions and more efficient loss frequency of dust, respectively, which is
362 discussed in detail in the later sections. Over the ocean domain, the magnitude of
363 GOCART DOD (0.05) is in between the MODIS-derived DOD (0.06) and CALIOP-
364 derived DOD (0.03), whereas the other models obtain much smaller values (0.001-0.009).
365 Compared with the coarse-mode AOD (proxy of DOD) from AERONET, most models
366 (except GOCART) seem to significantly underestimate the dust transport from source
367 regions across the North Pacific.
368 Satellites indicate that f_{DOD} values vary depending on sensor type and region
369 ranging 0.27-0.36. The satellite mean f_{DOD} over land (0.39) is 0.11 greater than over
370 ocean (0.28). Models show large range of f_{DOD} both over land (0.11-0.42) and ocean
371 (0.007-0.29). The ensemble means of model AOD, DOD and f_{DOD} are 0.21, 0.05, 0.25
372 over land and 0.16, 0.02, and 0.1 over ocean, respectively (Table 4). The comparison
373 between satellite and model ensemble means again shows within 10 % differences in
374 AOD over land and ocean, but a factor of two low bias in model is shown for DOD and
375 f_{DOD} over ocean.
376
377 3.2 Longitudinal gradient
378 We examine the longitudinal gradient with the mean AOD and DOD from
379 satellites and models between 20°N and 60°N in 5° longitude intervals between 60°E-
380 120°W (Figure 4a). MODIS shows the highest AOD (0.47) at 115°E-120°E, whereas
381 MISR and CALIOP have the peaks in the same location but with lower values (0.29 and
382 0.35, respectively). All satellite data show a gradually decreasing pattern eastward across

383 the Pacific Ocean (i.e., east of 140°E). The range of west-to-east AOD gradient between
384 140°E-120°W in MODIS (from 0.23 to 0.11, a factor of 2.1) is larger than that in MISR
385 (from 0.21 to 0.13, a factor of 1.6). The pattern of the CALIOP AOD gradient over ocean
386 (from 0.11 to 0.06, a factor of 1.8) is similar to that of MODIS and MISR, but the
387 magnitude of AOD is about half of other satellites. Differences in sampling and cloud-
388 masking account for much of the diversity in the satellite-derived AOD gradients. All
389 models capture the location of the maximum AOD over Eastern China, but some of them
390 miss the peak over the Indo-Gangetic Plain and Taklimakan. Although the magnitudes of
391 the decreasing longitudinal AOD gradients vary by model, all models show a decreasing
392 longitudinal gradient of AOD.
393 Over land, MODIS and CALIOP DOD over the Taklimakan and Thar deserts
394 (i.e., west of 85°E) are larger (0.19 and 0.14, respectively) than over the Gobi Desert and
395 Loess Plateau (0.14 and 0.1, respectively). All the models except GOCART show lower
396 DOD than CALIOP, especially ECHAM5 and HadGEM2, as the average DOD from
397 these two models is only 0.01-0.05 over land. Over ocean, MODIS and MISR show
398 similar decreasing DOD gradient from the west (0.10 and 0.07) to the eastern Pacific
399 (0.03 and 0.04), respectively. The decreasing gradient of CALIOP DOD from west (0.05)
400 to east Pacific (0.01) is only half the MODIS and MISR values. Overall, the satellites
401 show a 40-60 % decrease of AOD and 35-70% decrease of DOD during the long-range
402 transport from the Asian coast to the eastern North Pacific Ocean (i.e., 130°E-125°W).
403 Although most models except GOCART have lower DOD than MODIS by a factor of 3-
404 10 in the coastal region (i.e., 130°E), all models also show the decreasing DOD gradient,

405 which is clear when the data are normalized to their respective values at the Asian coast
406 (130˚E).
407 The CALIOP DOD fraction over land ($f_{DOD,}$ bottom panel in Figure 4a) is highest
408 (0.55) near 60°E; then it gradually decreases across the Pacific towards the east to 0.32 at
409 125°W. MODIS also show similar f_{DOD} gradient between west and east (i.e., 0.65 to
410 0.30). The satellite f_{DOD} values over ocean are close to each other, in the range of
411 0.24~0.34, across the Pacific. The maximum f_{DOD} values from the models near 60°E are
412 spread by a factor of two (0.28~0.57), and most models seem to show much faster f_{DOD}
413 decrease from west to east over land (a factor of 3-4 decrease) than the satellites and the
414 GOCART model. Over ocean, the mean f_{DOD} values from the models show a large (factor
415 of 30) difference, from 0.01 (ECHAM5) to 0.29 (GOCART), and the latter is the closest
416 to the satellite data.
417 When normalized to the value at 130°E, satellites estimate a 38-59 % AOD
418 decrease, and a decrease of 34-69 % for DOD, during trans-Pacific transport (Figure 4b).
419 The increasing gradient of MISR f_{DOD} is due to the steeper gradient in DOD than AOD,
420 although its physical explanation needs more investigation. In contrast, models show a
421 wider range of decreasing longitudinal gradients: 42-69 % for AOD and 44-88 % for
422 DOD. The normalized AOD gradient from the models is generally similar to that from
423 satellites, although GISS and ECHAM5 show an increase of AOD in the middle of the
424 Pacific Ocean (160°E-150°W). By contrast, the longitudinal gradients of normalized
425 DOD and f_{DOD} are much more spread out in the satellite data and models, revealing large
426 discrepancies (a fact or of 4) not only between the satellites over the North Pacific, where

AOD and DOD are relatively low, but also among models in dust transport and removal processes.

Overall, all satellites show a gradual decrease of AOD and DOD eastward during trans-Pacific transport. They show that 40-60% of AOD and 30-65% of DOD reach the eastern Pacific from the Asian coast. Models capture the decreasing gradient of the satellite AOD and DOD; however, most models except GOCART largely underestimate DOD and f_{DOD} over ocean.

3.3 Seasonal cycle and inter-annual variability

The seasonal variation of multiyear mean AOD and DOD for land and ocean are shown in Figures 5 and 6, respectively. The seasonal variability of the three satellite AODs agree with each other over land (Figure 5), showing high AOD during April-July and low AOD between October and January. MODIS AOD (0.17-0.37) is higher than MISR and CALIOP by 0.06 to 0.07. The seasonal variation of MODIS and CALIOP DOD is similar to that of AOD with the peak in April (0.21 and 0.14, respectively). The f_{DOD} is highest in March-April (0.46-0.50) for MODIS and CALIOP, and lowest in December-January (0.27-0.28) in MODIS and July-August (0.33) in CALIOP.

Models also show strong seasonal variability over land; however, only GOCART shows the AOD and DOD maxima in April, reproducing the seasonal cycles in the satellite data. The other models shift the seasonal maximum to the boreal summer months. The differences between the modeled AODs range from 0.06~0.07 in winter to 0.18 in April. GOCART resembles closely the magnitude of MODIS, whereas the other models simulate AOD values similar to MISR and CALIOP. The maximum DOD in

450 GOCART, GISS and SPRINTARS ranges from 0.12-0.22, which is comparable to
451 satellites (0.14-0.21). Interestingly, despite the large differences in seasonal variation
452 among the models, they all consistently show a maximum f_{DOD} in April, even though the
453 values differ by a factor of 2, from 0.3 in ECHAM5 to 0.6 in GOCART, which can be
454 compared to the CALIOP f_{DOD} maximum of 0.5 in spring. Overall, the models capture
455 the magnitude of the satellite AOD over land, but the seasonality differs; apparently,
456 reproducing the magnitude of the observed DOD is more difficult.
457 Over ocean, there are clear discrepancies among the satellite data. Although the
458 seasonal variability and magnitude of AOD from MODIS and MISR agree with each
459 other (Figure 6) as both showing the highest AOD (0.28 and 0.26, respectively) in April-
460 May, the CALIOP AOD is quite different not only in seasonal variation (maximum AOD
461 from January through April and a minimum in August), but also in magnitude (about a
462 factor of 2 lower). Discrepancies of similar magnitudes are found for satellite-derived
463 DOD and f_{DOD} as well, with the largest difference appearing in the summer. Both MISR
464 and CALIOP display DOD and f_{DOD} minima in July, a feature that is lacking in the
465 MODIS data. As noted in Section 2, sensitivity to the proxies used to identify the DOD
466 component in the satellite retrievals diminishes when the AOD is low.
467 Model simulations over the ocean also show large discrepancies. Although the
468 AOD seasonal variation from GOCART (0.27) closely follows that from MODIS and
469 MISR with a maximum AOD (0.26-0.28) in April-May, GISS and ECHAM5 indicate a
470 maximum AOD in winter (0.21-0.25) and a minimum AOD (0.12) in summer, which is
471 also out of phase with the seasonal cycle simulated by SPRINTARS and HadGEM2. The
472 largest DOD and f_{DOD} differences over ocean among the models appear between

GOCART and ECHAM5: GOCART-simulated DOD (f_{DOD}) over the North Pacific varies from 0.02 (0.2) in winter to 0.14 (0.48) in April, similar to the corresponding values from MODIS, whereas these fields from ECHAM5 are below 0.03 (Figure 6, right-bottom panel). Overall, the DOD and f_{DOD} diversity among the models is huge, with differences up to a factor of twenty. The same result is obtained when the analysis is conducted over the smaller domains (Figures S3-S5).

Overall, most models, except for GOCART, strongly underestimate the magnitude of DOD over ocean, relative to the satellite results. The absence of dust over ocean in these models produces large differences in ocean-AOD seasonality, with peaks in summer or winter that disagree with the MODIS and MISR AOD. In addition, the AOD and DOD differences between MODIS, MISR, and CALIOP over ocean highlight the challenge of DOD observation in the Northern Pacific region. We will discuss the differences presented by the CALIOP DOD further in later sections.

3.4 Vertical distribution of aerosol and dust

The vertical profiles of modeled aerosol and dust are compared with CALIOP profiles averaged over 2007-2011. Considering the spatial variability within the large domain, we chose six sub-domains (Figure 1); three domains include major dust source regions over the Thar desert (THAR, 70°E-75°E; 25°N-30°N), the Taklimakan desert (TAKL, 75°E-90°E; 35°N-45°N), and the Gobi desert (GOBI, 95°E-115°E; 40°N-45°N), and three sub-domains across the Pacific capture the trans-Pacific transport of aerosol and dust [NWP (135°E-140°E; 25°N-50°N), NCP (175°E-180°E; 30°N-55°N), and NEP (130°W-125°W; 35°N-60°N)].

The comparison includes the area-averaged vertical profiles of extinction coefficients for total aerosol (σ_{aer} in km^{-1}) and dust (σ_{du} in km^{-1}), and the ratio of dust extinction to total aerosol extinction from the surface up to 12 km (Figure 7-8). We also compare the height representing the center of aerosol extinction (Z_α) in each vertical column, following Koffi et al. (2012), such that $Z_\alpha = \frac{\sum_{i=1}^{k}(b_{ext,i} \cdot z_i)}{\sum_{i=1}^{k} b_{ext,i}}$, where k is the total number of layers in each column and $b_{ext,i}$ is extinction coefficient for layer i within the column.

The sub-domain-averaged CALIOP vertical profiles calculated with both "including clear-air" (solid black line) and "excluding clear-air" (dashed black line) are plotted in Figures 7-8 together with the corresponding profiles from the models. The column-integrated AOD and DOD, and the extinction-weighted height, are listed on each panel. In the present section, we focus on the "including clear-air" case of the CALIOP averaged data (described in section 2.2.1); the results for the "excluding clear-air" case are covered subsequently, in the discussion section. We present the result for the spring season between March and May, as CALIOP and the models have stronger aerosol and dust signals during spring in five out of six sub-regions over the sources and the ocean, except for THAR, which has its peak during summer.

Over the dust source regions of THAR, TAKL, and GOBI, the CALIOP observations show a layer of total aerosol and dust extending from the surface to the middle troposphere (~6 km) during the spring season (Figure 7). The CALIOP profiles show different maximum extinction values among these regions, ranging 0.09-0.11 km^{-1} for total aerosol and 0.04-0.06 km^{-1} for dust. The peak aerosol extinction appears near the surface in THAR, but is more elevated in TAKL and GOBI (i.e., 1.0-2.0 km). The

519 extinction-weighted average height of total aerosol ($Z_{\alpha,aer}$) from CALIOP (2.06-2.59 km)
520 is about 0.1-0.4 km lower than that of dust aerosol ($Z_{\alpha,du}$) (2.17-2.97 km), suggesting that
521 even near these source regions, dust tends to reside higher in the atmosphere than other
522 aerosols. The column-integrated AOD and DOD vary with location, between 0.27-0.30
523 and 0.13-0.18, respectively. In contrast, a clear and significant contribution of dust to
524 total aerosol extinction (f_{DOD}>0.5) appears at most altitudes over all sub-regions. The
525 strong negative bias near the surface is due to a signal artifact that occurs when the level
526 1B attenuated backscatter becomes strongly negative, preceding a strongly scattering
527 target such as the surface (Winker et al. 2009, 2013; Tackett et al., 2018).
528 There is a large spread in model-simulated aerosol and dust extinction vertical
529 distributions over the dust source regions in spring (Figures 7). Most models show a
530 maximum value of total aerosol and dust extinction at or near the surface. The average
531 aerosol height (0.86<$Z_{\alpha,aer}$<2.01) and the average dust height (0.75<$Z_{\alpha,du}$<2.07) from the
532 models are about 1-2 km lower than CALIOP. Differences in AOD and DOD in the three
533 dust source regions also appear among the models. GOCART has the highest AOD over
534 TAKL (0.36), whereas other models have the highest AOD over THAR (0.21-0.35), and
535 CALIOP reports highest AOD over GOBI (0.30). For DOD, the highest values appear
536 over TAKL in GOCART (0.30), THAR in GISS (0.17), and GOBI in SPRINTARS
537 (0.30) and HadGEM2 (0.07); CALIOP finds essentially equal springtime DOD peak
538 values over TAKL and THAR (0.18). Figure 7 shows that HadGEM2 severely
539 underestimates the dust amount in THAR and TAKL. The shape of f_{DOD} between
540 CALIOP and models are very different, as CALIOP is consistent throughout the

atmosphere whereas the models show f_{DOD} decreasing with elevation. The magnitudes of the modeled f_{DOD} values are spread widely, showing large differences with CALIOP.

Over ocean (Figures 8), CALIOP displays a shallower aerosol and dust layer and lower extinction magnitudes compared to the features in the source regions. According to CALIOP, aerosol and dust are confined below 1 km in all ocean domains. Although the average aerosol height decreases by 0.5 km during long-range transport from NWP ($Z_{\alpha,aer}$ =2.27 km) to NEP ($Z_{\alpha,aer}$ =1.77 km), that of dust maintains at about the same level ($Z_{\alpha,du}$ = 2.49 km in NWP and 2.57 km in NEP). The CALIOP total-column AOD and DOD show strongly decreasing gradients from west to east (from 0.18 over NWP to 0.08 over NEP for AOD, from 0.07 over NWP to 0.03 over NEP for DOD). The f_{DOD} values (~0.5) over ocean are lower than over the land regions.

Large model diversity in aerosol and dust vertical profiles also appears over ocean (Figure 8). In general, total aerosol extinction peaks are located near the surface and decrease with altitude, except for GISS, which places a second aerosol layer around 2 km. However, the models show that dust extinction reaches maximum values in layers aloft, centered around 3 km, and then decreases with altitude. Consequently the averaged dust height $Z_{\alpha,du}$ (2.56-4.22 km) is significantly higher than the average aerosol height $Z_{\alpha,aer}$ (0.69-2.58 km). It is worth noting that $Z_{\alpha,du}$ of all models increases (from 2.56-3.38 km to 3.57-4.22 km) between NWP and NEP, in contrast with the nearly constant height reported by CALIOP, and the modeled $Z_{\alpha,du}$ values are up to 1.5 km higher than CALIOP in the ocean domains.

The comparison of vertical profiles showed that (1) CALIOP derives thick dust layers reaching up to 6 km over that dust source regions, and a shallower, weaker aerosol

and dust layer over ocean, whereas the models show a large spread in the vertical distribution of dust over both land and ocean; (2) the average height of dust in the models underestimates CALIOP over land, but they overestimate CALIOP over ocean; (3) $Z_{\alpha,du}$ of all models increases during long-range transport over ocean, whereas $Z_{\alpha,du}$ barely changes according to CALIOP; and (4) CALIOP shows large dust fraction throughout the domains, whereas there are wide differences (factors of a few or more) in dust fraction among models.

4. Diversity of dust emission, removal, and optical parameters among models

4.1 Model emissions and physical/optical parameters

In this section, we examine the model simulations of the dust budget and several internal parameters in the study domain to help diagnose the large diversity among models, including emission, dry and wet depositions, dust mass loading, loss frequency (LF, which is the removal rate divided by the dust mass loading), optical depth, and the mass extinction efficiency (MEE, which converts dust mass to extinction at 550 nm). The results are summarized in Table 4 and some are shown in Figures 9 and 10. For dust emissions, Figure 9 indicates that all models produce similar "hot spots", such as the Taklimakan desert, Gobi desert, Inner Mongolia, Thar desert, and the deserts in Central Asia. However, there are clear differences in locations and amounts of emission fluxes. GOCART and SPRINTARS show similar areas and emission rates in confined source locations in China, but they differ considerably for locations in India and central Asia. Dust emissions in other models are more spatially spread out but the emission rates are much lower than GOCART and SPRINTARS. Note that differences in dust emission

587 between models are determined not only by the emission parameterization scheme and
588 meteorology, but also by the particle size distribution and the size range. However, the
589 AeroCom database only contains total dust emissions without size-segregated
590 information. The lowest mass emission is in ECHAM5 (77.4 Tg yr^{-1}), which considers
591 smaller size particles in its modal approach (0.05-0.5 μm in radius). SPRINTARS and
592 GOCART have the same maximum size of 10 μm (radius), but SPRINTARS emission
593 (825.9 Tg yr^{-1}) is 21% larger than GOCART (680.5 Tg yr^{-1}). GISS (200.4 Tg yr^{-1}) and
594 HadGEM2 (488.8 Tg yr^{-1}) have maximum size larger than 10 μm (radius), but their
595 emissions are lower than GOCART and SPRINTARS (see Table 4). Overall, the domain
596 dust emission among models differs by more than a factor of 10, from 77.4 Tg yr^{-1} in
597 ECHAM5 to 825.9 Tg yr^{-1} in SPRINTARS. The comparison here suggests that the
598 differences in dust size-range alone cannot explain the diversity in dust emissions
599 between the models. Rather, the dust uplifting mechanisms and/or meteorological
600 conditions (e.g., winds, soil wetness) might also play a role in the dust emission
601 differences among the models.
602 We compare three physical and optical parameters from the models in our study
603 domain: loss frequency (LF in day^{-1}), which is the total dust deposition rate (sum of wet
604 and dry deposition rates) divided by the dust mass loading; f_{wet}, which is the dust wet
605 deposition fraction of total deposition, and the dust mass extinction efficiency (MEE in
606 m^2g^{-1}), which is the ratio of DOD to dust mass loading (Figure 10). The mean values of
607 these parameters for each region per model are summarized in Table 4.
608 During long-range transport, aerosol loading and consequently LF are affected by
609 advection and deposition as well as by particle size distribution. The range of the annual

610 mean LF values over the land and ocean domains among the models range between 0.20-
611 0.53 and 0.09-0.21 day^{-1}, respectively (Table 4 and Figure 10a). SPRINTARS and
612 HadGEM2 show higher LF (> 0.9 day^{-1}) in and around their respective source locations,
613 indicating that dust aerosols are quickly removed before transport far from the source
614 region occurs, due to the effective settling of large particles. GOCART and GISS show
615 relatively lower LF (< 0.7 day^{-1}) over source regions. ECHAM5, which allows dust to
616 mix with other aerosols internally, shows low LF (< 0.5 day^{-1}) in and near source regions,
617 but it has high LF (> 0.9 day^{-1}) outside the deserts over land. The highest LF (>0.9 day^{-1})
618 in the Tibetan Plateau in ECHAM5 is explained by stronger wet-removal than other
619 models. ECHAM5 has the highest LF, which explains why the steepest decreasing DOD
620 gradient shown in Figure 4b corresponds to that model. All models show lower LF (<0.4
621 day^{-1}) in 20°N-60°N over ocean than near-source (over land).
622 Dust from the Taklimakan and Gobi Deserts is frequently to be transported
623 toward the North Pacific. The highest emission from these regions is in GOCART (462.3
624 Tg $year^{-1}$), followed by SPRINTARS (374.6 Tg $year^{-1}$), HadGEM2 (134.7 Tg $year^{-1}$),
625 GISS (81.6 Tg $year^{-1}$), and ECHAM5 (26.1 Tg $year^{-1}$) (Table S2). The contribution from
626 these regions to the total domain emission is higher in GOCART (68 %) than other
627 models (28 % in HadGEM2 ~ 45 % in SPRINTARS). Dust emission from the
628 Taklimakan is factor of a few higher in GOCART (252.9 Tg $year^{-1}$) and SPRINTARS
629 (208.6 Tg $year^{-1}$) than other models (0.1~31.2 Tg $year^{-1}$). Similarly, GOCART and
630 SPRINTARS DOD better agrees with MDB DOD over the Taklimakan Desert, whereas
631 other models are understated (Figure S6). The result indicates that the higher DOD (0.08)
632 in GOCART over the Northern Pacific is attributed by the combined effects of lower loss

frequency (0.15 day^{-1}) and higher emission. In contrast, dust emission in SPRINTARS is higher than GOCART but its mean DOD (0.05) is 33.5 % lower than GOCART, mainly due to the high loss frequency (0.26 day^{-1}) in SPRINTARS. Other models have much lower emissions than GOCART and SPRINTARS.

The models in the present study include two major deposition processes to remove dust aerosols from the atmosphere: dry (including gravitational settling and aerodynamic deposition) and wet (including convective scavenging and large-scale rainout/washout), and their efficiencies are highly model-dependent. The distributions of wet deposition fraction over total deposition, f_{wet} between models are compared in Figure 10b. For major dust source regions over land, all models give consistently low f_{wet} values of less than 0.1, since total dust removal is dominated by gravitational settling of larger particles near the source. The f_{wet} increases away from the source over land (>0.9 in GISS, ECHAM5, and HadGEM2, and 0.5~0.6 in the other models). Over the Pacific Ocean, the models show substantially higher f_{wet}, with the highest f_{wet} (0.92) in HadGEM2 and the lowest in GOCART (0.62), resulting in a 48 % relative difference between the two. The annual mean precipitation over the North Pacific Ocean ranges from 2.86 (mm day^{-1}) in SPRINTARS to 3.49 (mm day^{-1}) in GISS, and the precipitation field has a peak in summer in all models (Figure S7). The order of f_{wet} between models is not consistent with the order of precipitation, due to differences in the modeled wet and dry removal processes. Overall, GOCART LF along the dust transport route over ocean is also the lowest, resulting in the highest DOD among models, and it actually agrees best with the satellite data.

655 Although MEE is the extinction efficiency per unit mass, it is also affected by
656 both particle size distribution and the optical properties adopted by the models (e.g., mass
657 extinction coefficient is higher for fine-mode particles than coarse-mode particles). All
658 models show that dust MEE is lower over source regions (0.3-0.8) than downwind
659 towards the eastern Pacific Ocean, consistent with the notion that dust particle size is
660 larger near the source, and that large particles are more efficiently removed than the fine
661 particles. The mean MEE (m^2g^{-1}) among models ranges from 0.57 (GOCART) to 1.01
662 (SPRINTARS) over land, and from 0.61 (GOCART) to 1.12 (SPRINTARS) over ocean
663 (Table 4). Overall, the spatial distribution of dust MEE is particle-size dependent, ranging
664 from 0.3-0.7 in GOCART to 0.7-1.3 in SPRINTARS, with SRINTARS' dust MEE
665 overall about 80% larger than GOCART.
666 We estimate the model diversity (Table 4), which is defined as the ratio of the
667 standard deviation of the model results to the multi-model mean (Textor et al., 2006).
668 Over the full domain, diversity for the mass-related parameters (*i.e.*, emission, mass
669 loading, dry deposition, and wet deposition) is in the range of 39-100 %. Diversity for the
670 optical parameters of AOD and DOD is 10 and 84 %, respectively, indicating models
671 experience more uncertainty in representing dust mass and DOD than AOD.
672 Inter-model comparison in this section allows us to explain the large diversity of
673 DOD (i.e., 84%); dust mass loading and mass extinction efficiency are the determining
674 factors for DOD estimation. The diversity of LOAD (100%) is among the largest in the
675 analyzed parameters, mainly due to the combined effects of EMI (69%), DRY (72%), and
676 WET (39%). In comparison, the diversity of MEE is much smaller (23%), suggesting that
677 the diversity of DOD is determined mainly by the diversity of LOAD. For EMI, each

678 model uses its own parameterization scheme, input surface condition, and surface wind
679 speed, generating large differences among models. Each model uses a different
680 parameterization scheme for DRY and WET processes, resulting in 31% diversity in LF.
681 Differences in meteorological fields between models such as wind, precipitation, and
682 circulation also contribute to the diversity of dust lifetime. Further, different optical tables
683 and size distributions among models is an important factor for dust removal process and
684 optical property calculation.

685 A critical question in this study is which factor among emission, removal, and
686 optical property is more responsible for contributing to the diversity of the AeroCom
687 model simulated DOD? To answer the question, we have calculated a partial sensitivity
688 of DOD to the above model parameters, based on the method in Schulz et al. (2006).
689 Since DOD is determined by the dust load (LOAD) and mass extinction efficiency
690 (MEE), and the LOAD is determined by the source (SRC) and the deposition removal
691 rate (expressed as residence time RES, which is reciprocal of LF), the domain averaged
692 DOD can be expressed as: DOD = SRC (g m^{-2} s^{-1}) × RES (s) × MEE (m^2 g^{-1}).
693 Because of the study domain is not global such that the dust emission is not necessarily
694 balanced by the deposition term averaged over the study time period (several years) and
695 domain, the net SRC is thus expressed as SRC = EMI + (EMI-DEP). For each model *n*,
696 the DOD sensitivity with respect to factor *x* is defined as: $DOD_{x,n} = x_n/\langle x\rangle \times \langle DOD\rangle$,
697 where <*x*> is the multi-model mean of *x* and <DOD> is the multi-model mean DOD.
698 Figure 11 shows the partial sensitivity of DOD to the net SRC, RES, and MEE for the
699 five AeroCom models, with the last two points showing the DOD from each model and
700 satellite. For reference, the partial sensitivity of DOD to EMI within the domain is shown

as “x” symbol for each model; the difference between the SRC and EMI is the net dust imported to the domain if SRC>EMI or export from the domain if SRC<EMI.

Comparing GOCART and SPRINTARS, the shorter residence time (i.e. the higher loss frequency) in SPRINTARS is likely to be responsible for the lower simulated DOD in SPRINTARS, despite higher dust source and higher MEE in SPRINTARS. The low DOD in GISS and ECHEM is most likely driven by the low dust source (low emission rates and net export). It is interesting that HadGEM2 shows much higher dust source (EMI + net import) than GISS but comparable residence time (or loss frequency) and MEE with GISS, but its simulated DOD is significantly lower than GISS, which is difficult to explain without more detailed information, such as size-segregated emission and optical properties. Overall, the result in Figure 11 shows that the diversity of DOD is mostly driven by the diversity of the dust source followed by that of the residence time, and to a less extent by the differences in MEE.

Among the five models, GOCART agrees with the satellite data the best in terms of DOD over land and ocean, transpacific DOD gradient, and seasonal cycle. However, there is still a lack of observational data to validate or constrain the emission, dry and wet removal (the slowest among models), and MEE (the lowest among models) in GOCART. We can only say that the combination of these factors allows GOCART to simulate the DOD magnitude, horizontal distributions, and seasonal variations that are the closest to the satellite observations.

4.2 Comparison with North African dust

723 To address how model-simulated dust over the Asia-Pacific Ocean compares with
724 North Africa-Atlantic Ocean, we compare AOD and five dust physical and optical
725 parameters (DOD, f_{DOD}, f_{wet}, LF, and MEE) from the current study with our previous
726 study over North Africa and the Atlantic Ocean (i.e., Kim et al., 2014) (Figure 12 and
727 Table 5). In the comparison, each parameter from the models is averaged over land and
728 ocean to simplify the discussion.
729 Due to the differences in dust size and meteorology in the source regions, dust
730 emission and DOD over North Africa (1048 Tg yr^{-1} and 0.18, respectively) is 2~3 times
731 larger than over Asia (454 Tg yr^{-1} and 0.05). The models show a factor of two difference
732 in f_{DOD} between North Africa (0.52) and Asia (0.25), indicating that other pollutants play
733 a more important role over Asia. Dust LF is comparable between the two continents
734 (about 10%), with that over North Africa (0.39 day^{-1}) slightly larger than over Asia (0.36
735 day^{-1}). Considering the spectral dependency of dust particle size, the lower dust MEE
736 between North Africa (0.65 m^2g^{-1}) and Asia (0.73 m^2g^{-1}) suggests larger dust particle size
737 over North Africa than Asia. The higher f_{wet} over Asia (0.55) than over North Africa
738 (0.32) reflects more frequent and abundant precipitation over Asia than North Africa. The
739 comparison between the Atlantic and Pacific Oceans shows a similar pattern as in North
740 Africa and Asia (Figure 12b). Furthermore, the longitudinal gradient of the trans-Pacific
741 dust is about one-half of the trans-Atlantic dust, due to higher dust elevation and
742 differences in precipitation.
743 AeroCom models use the same anthropogenic emissions, but dust emission is
744 calculated by each model. As a result, the diversity of model AOD over the more polluted
745 Asia region (13%) is much smaller than that for North Africa (50%). However, the

746 diversity of DOD (66-75%) is larger for Asia and North Africa than diversity of AOD.
747 Over ocean, the AOD diversity for the Pacific Ocean (21%) is smaller than for the
748 Atlantic Ocean (34%), but the diversity of DOD for the Pacific Ocean (121%) is three
749 times as large as for the Atlantic Ocean (45%), due to the differences in meteorological
750 fields and removal processes. Diversities of other physical and optical parameters
751 between North Africa and Asia are low and comparable, with differences generally less
752 than 10%.
753
754 5. Discussion
755 The present inter-model dust comparison has shown that there are large
756 differences among models, among the satellite observations, and between models and
757 satellite observations. Among the five participating AeroCom models, most of them
758 except GOCART significantly underestimate DOD relative to the satellite-derived values
759 over Asia and the Pacific Ocean, whereas GOCART emits more dust (i.e., 2nd most dust
760 emission after SPRINTARS) and shows longer dust lifetime during transit. The
761 participating models have different size range and thus they have different size
762 distributions as reflected in Table 1. Recent studies have shown that the wide spread in
763 size-distribution between models, and in addition models generally simulate too much
764 fine dust compared to observations (Kok et al., 2017). The differences in emission, size
765 distribution and dry deposition efficiency (i.e., the ratio of DRY to EMI in Table 4)
766 between models contribute to the large diversity in DRY between models. The aerosol
767 size distribution is a subject of future inter-model comparison studies.

In summary, the analysis of model diversity for various physical/optical parameters raises the following points: (1) Among the mass-related parameters (emission, load, dry and wet deposition), the greatest diversity appears in the dust mass loading, especially over ocean. (2) The diversity of dry deposition is about twice larger than that of wet deposition. (3) There is a sharp contrast between the diversity of AOD and that of DOD, i.e., the diversity of AOD is only 12-17% of the diversity of DOD. (4) The diversity of almost all parameters over ocean is larger than the corresponding quantities over land. (5) The diversity of DOD is mostly driven by the diversity of the dust source followed by that of the residence time, and to a less extent by the differences in MEE.

As presented in section 3, we assigned CALIOP aerosol extinction in "clear-air" a value of 0 km^{-1} following the method described in section 2.2.1. CALIOP data using this method agrees with MODIS and MISR for AOD, and MODIS for DOD over land. However, this causes a low bias in averaged aerosol vertical profiles and thus underestimates AOD and DOD relative to MODIS and MISR, especially over ocean. As constraining aerosol extinction below the detection limit is highly uncertain, we also provide an upper bound on the extinction profiles by excluding the "clear-air" data in the average. If we exclude the clear-air data in the average, it removes much of the sampling, approximately 70 % over dust source regions and 90 % over remote ocean (Figure S1f). The "excluding clear-air" case does not alter the AOD and DOD horizontal patterns and their longitudinal gradients much. However, the AOD and DOD magnitudes are 70-80 % larger than the "including clear-air" case over land and ocean (Figure 13, left panel and Table 6). Actually, in the "excluding clear-air" case, the CALIOP longitudinal gradients agree better with the other satellites over ocean, but the resulting CALIOP AOD and

791 DOD over land is larger than the other satellites (Figure 13, right panel). Overall, the
792 effects of how "clear-air" is represented produces large differences in AOD and DOD
793 over land and ocean, yet the change to f_{DOD} is less than 10%.

794 The impact of how "clear-air" is represented on the shape and magnitude of the
795 CALIOP vertical profiles is large (solid and dashed lines in black in Figures 7-8). Over
796 the land domains, the aerosol and dust extinctions of the "excluding clear-air" case are
797 about twice as large as the "including clear-air" case at all altitudes. Also, the average
798 heights (Z_{α}) increase by 0.4-0.9 km for total aerosol and 0.6-1.0 km for dust. Over the
799 ocean domains, aerosol extinctions for the "excluding clear-air" case are about 3-5 times
800 larger and $Z_{\alpha,aer}$ is about 1.2-1.8 km higher than the "including clear-air" case. Dust
801 extinction for the "excluding clear-air" case is 2-5 times larger, and $Z_{\alpha,du}$ is about 1.4-1.8
802 km higher, than the "including clear-air" case. These results suggest that the low
803 detection limit of CALIOP may miss large amount of background aerosol and dust signal,
804 which is consistent with a previous study (Watson-Parris et al., 2018). Given the
805 limitations and uncertainties in the CALIOP vertical profiles over ocean, where the
806 aerosol amount is low, it is difficult to use the CALIOP data to meaningfully evaluate the
807 model-simulated vertical profiles.

808 Finally, our study shows that satellite remote sensing is crucial to better
809 understand the large-scale distribution and variation of dust. Although the three satellite
810 data sets considered show general agreement of AOD and DOD patterns, they also leave
811 large uncertainties in estimating aerosol and dust over Asia and especially over Pacific
812 Ocean due to 1) the presence of sea-spay aerosol and clouds, 2) mixing of dust with other
813 continental aerosol, and 3) data sampling biases and instrument sensitivity limitations.

Our study emphasizes that better aerosol and dust detection over the Pacific Ocean is essential to reduce the uncertainty inherent in the present study.

6. Summary

We evaluated dust and total aerosol over Asia and the North Pacific Ocean for five AeroCom II global models by comparing the model-simulated spatial and temporal distributions with a suite of satellite remote-sensing data and with AERONET sun photometer measurements. Our evaluation targeted four areas: (1) spatial distributions of AOD and DOD over Asia and the North Pacific Ocean, (2) longitudinal gradient of AOD and DOD during trans-Pacific transport, (3) seasonal variations of AOD and DOD, and (4) vertical extinction profiles of total aerosol and dust. To understand the inter-model differences in the dust simulations, we also compared several key model parameters, including dust emission, dry and wet deposition, loss frequency, and dust mass extinction efficiency.

The satellites agree that high AOD exists over major pollution regions, and gradually decreases downwind from the source regions. They show a peak in spring and a minimum in winter. Over land, satellite observations of DOD are derived from MODIS (0.11) and CALIOP (0.09), which shows a large dust contribution over land, accounting for 36% and 42% of the total AOD, respectively. Over ocean, satellite observations show that the average AOD is more than half (62%) the value over land, and DOD derived from MODIS, MISR, and CALIOP accounts for 27-30% of AOD. It is worth noting that AOD and DOD of MODIS and MISR are close each other, but CALIOP is much lower

836 than the other satellites over the ocean domain. Overall, satellites show a 35-70 %
837 decrease of DOD from the west Pacific to the east Pacific.
838 Large differences among models and between models and observations were
839 found in all categories (column AOD/DOD, longitudinal gradient, seasonal variations,
840 and vertical profiles) in this analysis. The mean AODs from models are within 20 % of
841 the satellites; however, the inter-model differences over both land and ocean are
842 comparable to the inter-satellite instrument differences. On the other hand, most models
843 except GOCART underestimate DOD (0.00-0.05) compared to the satellite-derived
844 products (0.03-0.06). The models show a wide range of decreasing longitudinal gradients
845 for AOD (42-69 %) and DOD (45-88 %) across the Pacific Ocean, although the range is
846 comparable to the differences between satellite products (35-70%). The models show
847 large seasonal variations of AOD over land and ocean with a peak in spring or summer
848 (0.2-0.35) and a minimum in winter (0.1-0.2) over land and ocean. The DOD and f_{DOD}
849 differences among the models are very large, as high as a factor of 20. The models also
850 show peak DOD in spring and summer (0.05-0.24) and winter minima (<0.07).
851 The vertical profiles of CALIOP show thick dust layers up to 6 km over dust
852 source regions, and a shallower and weaker aerosol and dust layer over ocean. The
853 models display a large spread in dust vertical distributions over land and ocean; they
854 underestimate average height of CALIOP over land, but they overestimate over ocean.
855 $Z_{\alpha,du}$ according to CALIOP barely changes during long-range transport; in contrast, the
856 modeled $Z_{\alpha,du}$ increases during transport. Large dust fraction is detected from CALIOP
857 throughout the domain, whereas dust fraction between models vary widely, showing
858 factors of a few differences.

The differences in dust emissions among models are larger than a factor of 10 (77.4-825.9 Tg yr^{-1}) due to differences in source area size, dust size range, and meteorology, with a diversity value of 69%. The inter-model comparison also shows large diversity for mass-related parameters (*i.e.*, LOAD, DRY, and WET; 39-100 %), which explains the large diversity of DOD (84%). The diversity for dry deposition is about twice larger than that for wet deposition. The comparisons show that the AOD diversity is only 12-17% of the DOD diversity. Overall, for most parameters, the diversity over ocean is larger than over land.

While GOCART agrees with the satellite data the best in terms of DOD, there is still a lack of observational data to validate the emission, dry and wet removal rates (the slowest among models), and MEE (the lowest among models) in GOCART. For the same reason, it is difficult to point out specific causes for other models' underestimate the DOD in our study domain. Observation-based estimates on these quantities are needed for future progress in modeling dust aerosols in the atmosphere.

Acknowledgements

This work is supported by NASA Atmospheric Composition: Modeling and Analysis (NNH14ZDA001N-ACMAP) and EOS Programs. HY acknowledge the NASA support via NNH15ZDA001N-CCST and NNH17ZDA001N-TASNPP. We thank to Dr. Paul Ginoux for his insightful comments including MODIS Deep Blue dust optical depth. We would like to thank the MODIS, MISR, CALIOP, and AERONET teams for the data used in this study. Resources supporting this work were provided by the NASA High-End Computing (HEC) Program through the NASA Center for Climate Simulation (NCCS) at

882 Goddard Space Flight Center. Model data are available at the AeroCom webpage
883 (http://aerocom.met.no/). AERONET data is obtained from NASA AERONET webpage
884 (https://aeronet.gsfc.nasa.gov/). The MODIS Dark Target aerosol data were obtained from
885 the NASA Level-1 and Atmosphere Archive and Distribution System (LAADS) webpage
886 (https://ladsweb.nascom.nasa.gov/). The CALIOP aerosol products were obtained from
887 NASA Langley Research Center Atmospheric Science Data Center
888 (https://eosweb.larc.nasa.gov/).
889

References

Anderson, T. L., Wu, Y., Chu, D. A., Schmid, B., Redemann, J., and Dubovik, O. (2005), Testing the MODIS satellite retrieval of aerosol fine-mode fraction, J. Geophys. Res., 110, D18204, doi:10.1029/2005JD005978.

Balkanski, Y. J., D. J. Jacob, G. M. Gardner, W. C. Graustein, and K. K.Turekian (1993), Transport and residence times of tropospheric aerosols inferred from a global three-dimensional simulation of 210Pb, J. Geophys. Res., 98(D11), 20,573–20,586.

Bauer, S. E., and D. Koch (2005), Impact of heterogeneous sulfate formation at mineral dust surfaces on aerosol loads and radiative forcing in the Goddard Institute for Space Studies general circulation model, *J. Geophys. Res*., 110, D17202, doi:10.1029/2005JD005870.

Bellouin, N., J. Rae, A. Jones, C. Johnson, J. Haywood, and O. Boucher (2011), Aerosol forcing in the Climate Model Intercomparison Project (CMIP5) simulations by HadGEM2-ES and the role of ammonium nitrate. *J. Geophys. Res*., 116, D20206, doi:10.1029/2011JD016074.

Chin, M., et al. (2002), Tropospheric aerosol optical thickness from the GOCART model and comparisons with satellite and Sun photometer measurements, *J. Atmos. Sci*., 59, 461–483.

Chin, M., T. Diehl, P. Ginoux, and W. Malm (2007), Intercontinental transport of pollution and dust aerosols: implications for regional air quality, Atmos. Chem. Phys., 7, 5501-5517, https://doi.org/10.5194/acp-7-5501-2007.

Chin, M. et al. (2014), Multi-decadal aerosol variations from 1980 to 2009: a perspective from observations and a global model, Atmos. Chem. Phys., 14, 3657-3690, doi:10.5194/acp-14-3657-2014.

Chin, M., T. Diehl, O. Dubovik, T. F. Eck, B. N. Holben, A. Sinyuk, and D. G. Streets (2009), Light absorption by pollution, dust and biomass burning aerosols: A global model study and evaluation with AERONET data, *Ann. Geophys.*, *27*, 3439-3464.

Colarco, P., A. da Silva, M. Chin, and T. Diehl (2010), Online simulations of global aerosol distributions in the NASA GEOS-4 model and comparisons to satellite and ground-based aerosol optical depth, J. Geophys. Res., 115, D14207, doi:10.1029/2009JD012820.

Creamean, J. M., et al. (2013), Dust and biological aerosols from the Sahara and Asia influence precipitation in the western U.S., Science, 339(6127), 1572–1578.

Dubovik, O., Smirnov, A., Holben, B. N., King, M. D., Kaufman, Y. J., Eck, T. F., and Slutsker, I. (2000), Accuracy assessments of aerosol optical properties retrieved from Aerosol Robotic Network (AERONET) Sun and sky radiance measurements, J. Geophys. Res., 105, 9791–9806.

Evan, A. T., A. K. Heidinger, R. Bennartz, V. Bennington, N. M. Mahowald, H. Corrada-Bravo, C. S. Velden, G. Myhre, and J. P. Kossin (2008), Ocean temperature forcing by

aerosols across the Atlantic tropical cyclone development region, *Geochem Geophy Geosy*, 9. Q05V04, doi:10.1029/ 2007GC001774.

Forster, P., et al. (2007), Changes in atmospheric constituents and in radiative forcing, *in Climate Change 2007: The Physical Science Basis, Contribution of Working Group I to the Fourth Assessment Report of the Intergovernmental Panel on Climate Change*, edited by S. Solomon et al., pp. 129–234, Cambridge Univ. Press, Cambridge, U. K.

Fuchs, N. A., 1964: The Mechanics of Aerosols. Pergamon Press, 408 pp.

Ginoux, P., et al. (2001), Sources and distributions of dust aerosols simulated with the GOCART model, *J. Geophys. Res*., *106*(D17), 20,255–20,273.

Ginoux, P., J. M. Prospero, T. E. Gill, N. C. Hsu, and M. Zhao (2012), Global-scale attribution of anthropogenic and natural dust sources and their emission rates based on MODIS Deep Blue aerosol products, Rev. Geophys., 50, RG3005, doi:10.1029/2012RG000388.

Giorgi, F., and W. L. Chameides (1986), Rainout lifetimes of highly soluble aerosols and gases as inferred from simulations with a general circulation model. J. Geophys. Res., 91, 14 367–14 376.

Guo, Y., B. Tian, R.A. Kahn, O.V. Kalashnikova, S. Wong, and D.E. Waliser (2013), MJO-related Atlantic Dust and Smoke Variability in MODIS and MISR Satellite Observations. *J. Geophys. Res. 118,* doi:10.1002/jgrd.50409.

Hayasaka, T., S. Satake, A. Shimizu, N. Sugimoto, I. Matsui, K. Aoki, and Y. Muraji (2007), Vertical distribution andoptical properties of aerosols observed over Japan during the Atmospheric Brown Clouds - East Asia Regional Experiment 2005,J. Geophys. Res., 112, D22S35, doi:10.1029/2006JD008086.

Haywood, J. M., P. Francis, S. Osborne, M. Glew, N. Loeb, E. Highwood, D. Tanre, G. Myhre, P. Formenti, and E. Hirst (2003), Radiative properties and direct radiative effect of Saharan dust measured by the C-130 aircraft during SHADE: 1. Solar spectrum, *J. Geophys. Res*., 108(D18).

Holben, B. N., Eck, T. F., Slutsker, I., Tanre, D., Buis, J. P., Setzer, A., Vermote, E., Reagan, J. A., Kaufman, Y. J., Nakajima, T., Lavenu, F., Jankowiak, F., and Smirnov, A. (1998), AERONET – A federated instrument network and data archive for aerosol characterization, *Remote Sens. Environ*., 66, 1–16.

Hsu, NC, Tsay, SC, King, MD, Herman, JR (2004). Aerosol properties over bright-reflecting source regions, *IEEE Trans. Geosci. Remote Sens*., 42(3), 557-569.

Hu, Z., C. Zhao, , J. Huang, , L. R. Leung, , Y. Qian, , H. Yu, , L. Huang, , and O. V. Kalashnikova (2016), Trans-Pacific transport and evolution of aerosols: evaluation of quasi-global WRF-Chem simulation with multiple observations, *Geosci. Model Dev.*, 9, 1725-1746, https://doi.org/10.5194/gmd-9-1725-2016.

Huneeus, N., Schulz, M., Balkanski, Y., Griesfeller, J., Prospero, J., Kinne, S., Bauer, S., Boucher, O., Chin, M., Dentener, F., Diehl, T., Easter, R., Fillmore, D., Ghan, S., Ginoux, P., Grini, A., Horowitz, L., Koch, D., Krol, M. C., Landing, W., Liu, X., Mahowald, N., Miller, R., Morcrette, J.-J., Myhre, G., Penner, J., Perlwitz, J., Stier, P.,

971 Takemura, T., and Zender, C. S. (2011), Global dust model intercomparison in AeroCom
972 phase I, *Atmos. Chem. Phys*., 11, 7781-7816, doi:10.5194/acp-11-7781-2011.

973 Jickells, T. D., et al. (2005), Global iron connections between desert dust, ocean
974 biogeochemistry, and climate, *Science*, *308*, 67–71.

975 Kahn, R.A., D.L. Nelson, M. Garay, R.C. Levy, M.A. Bull, D.J. Diner, J.V. Martonchik,
976 S.R. Paradise, and E.G. Hansen, and L.A. Remer (2009), MISR Aerosol product
977 attributes, and statistical comparisons with MODIS. *IEEE Trans. Geosci. Remt. Sens 47*,
978 4095-4114

979 Kahn, R.A., B.J. Gaitley, M.J. Garay, D.J. Diner, T. Eck, A. Smirnov, and B.N. Holben,
980 (2010), Multiangle Imaging SpectroRadiometer global aerosol product assessment by
981 comparison with the Aerosol Robotic Network. *J. Geophys. Res*. 115, D23209, doi:
982 10.1029/2010JD014601.

983 Kahn, R. A., and B. J. Gaitley (2015), Ananalysis of global aerosol type asretrieved by
984 MISR, J. Geophys. Res. Atmos., 120, 4248–4281, doi:10.1002/2015JD023322.

985 Kalashnikova O. V., and R.A. Kahn (2006). Ability of multiangle remote sensing
986 observations to identify and distinguish mineral dust types: Part 2. Sensitivity over dark
987 water *J. Geophys. Res*., D11207, 111 10.1029/2005JD006756.

988 Kaufman, Y. J., I. Koren, L. A. Remer, D. Tanré, P. Ginoux, and S. Fan (2005), Dust
989 transport and deposition observed from the Terra-Moderate Resolution Imaging
990 Spectroradiometer (MODIS) spacecraft over the Atlantic Ocean, *J. Geophys. Res*., 110,
991 D10S12, doi:10.1029/2003JD004436.

992 Kim K.-M, W.-K. Lau, Y. C. Sud, and G. K. Walker (2010), Influence of aerosol-
993 radiative forcings on the diurnal and seasonal cycles of rainfall over West Africa and
994 Eastern Atlantic Ocean using GCM simulations, *Climate Dynamics*, 11, 115-126,
995 doi:10.1007/s00382-010- 0750-1.

996 Kim, M.-H., S.-W. Kim, S.-C. Yoon, and A. H. Omar (2013), Comparison of aerosol
997 optical depth between CALIOP and MODIS-Aqua for CALIOP aerosol subtypes over the
998 ocean, J. Geophys. Res.Atmos., 118, 13,241–13,252, doi:10.1002/2013JD019527.

999 Kim, D., M. Chin, H. Yu, T. Diehl, Q. Tan, K. Tsigaridis, S. E. Bauer, T. Takemura, L.
1000 Pozzoli, N. Bellouin, M. Schulz, S. Peyridieu, and A. Chédin (2014), Source, sinks, and
1001 transatlantic transport of North African dust aerosol: A multi-model analysis and
1002 comparison with remote-sensing data, *J. Geophy. Res. Atmos*., 119, 6259–6277,
1003 doi:10.1002/2013JD021099.

1004 Kinne, S., M. Schulz, C. Textor, S. Guibert, Y. Balkanski, S.E. Bauer, T. Berntsen, T.F.
1005 Berglen, O. Boucher, M. Chin, W. Collins, F. Dentener, T. Diehl, R. Easter, J. Feichter,
1006 D. Fillmore, S. Ghan, P. Ginoux, S. Gong, A. Grini, J. Hendricks, M. Herzog, L.
1007 Horowitz, I. Isaksen, T. Iversen, A. Kirkevåg, S. Kloster, D. Koch, J.E. Kristjansson, M.
1008 Krol, A. Lauer, J.F. Lamarque, G. Lesins, X. Liu, U. Lohmann, V. Montanaro, G. Myhre,
1009 J. Penner, G. Pitari, S. Reddy, Ø. Seland, P. Stier, T. Takemura, and X. Tie (2006), An
1010 AeroCom initial assessment optical properties in aerosol component modules of global
1011 models, *Atmos. Chem. Phys*., 6, 1815-1834.

1012 Koch, D., D. Jacob, I. Tegen, D. Rind, and M. Chin (1999), Troposphericsulfur
1013 simulation and sulfate direct radiative forcing in the Goddard In-stitute for Space Studies
1014 general circulation model,J. Geophys. Res.,104,23,799–23,822.

1015 Koffi, B., et al. (2012), Application of the CALIOP layer product to evaluate the vertical
1016 distribution of aerosols estimated by global models: AeroCom phase I results, *J.*
1017 *Geophys. Res*., 117, D10201, doi:10.1029/2011JD016858.

1018 Koffi, B., et al. (2016), Evaluation of the aerosol vertical distribution in global aerosol
1019 models through comparison against CALIOP measurements: AeroCom phase II
1020 results, *J. Geophys. Res. Atmos.*, **121**, 7254–7283, doi:10.1002/2015JD024639.

1021 Kok, J.F., D. A. Ridley, Q. Zhou, R. L. Miller, C. Zhao, C. L. Heald, D. S. Ward, S.
1022 Albani, and K. Haustein (2017), Smaller desert dust cooling effect estimated from
1023 analysis of dust size and abundance. Nature Geosci., 10, no. 4, 274-278,
1024 doi:10.1038/ngeo2912.

1025 Levy, R. C., Mattoo, S., Munchak, L. A., Remer, L. A., Sayer, A. M., Patadia, F., and
1026 Hsu, N. C. (2013), The Collection 6 MODIS aerosol products over land and ocean,
1027 Atmos. Meas. Tech., 6, 2989-3034, https://doi.org/10.5194/amt-6-2989-2013.

1028 Maher, B. A., Prospero, J. M., Mackie, D., Gaiero, D., Hesse, P., Balkanski, Y. (2010),
1029 Global connections between aeolian dust, climate and ocean biogeochemistry at the
1030 present day and at the last glacial maximum. 99, 1–2, 61–97.
1031 doi:10.1016/j.earscirev.2009.12.001.

1032 Miller, R. L., et al. (2006), Mineral dust aerosols in the NASA Goddard Institute for
1033 Space Sciences ModelE atmospheric general circulation model, *J. Geophys. Res*., 111,
1034 D06208, doi:10.1029/2005JD005796.

1035 Omar, A., Liu, Z., Vaughan, M., Thornhill, K., Kittaka, C., Ismail, S., et al. (2010).
1036 Extinction to backscatter ratios of Saharan dust layers derived from in situ measurements
1037 and CALIPSO overflights during NAMMA. Journal of Geophysical Research, 115,
1038 D24217. http://dx.doi.org/10.1029/2010JD014223.

1039 Pierce, J. R., R.A. Kahn, M. R. Davis, and J. M. Comstock, 2010. Detecting thin cirrus in
1040 Multiangle Imaging Spectroradiometer aerosol retrievals, *J. Geophys. Res., 115*, D08201,
1041 doi:10.1029/2009JD013019.

1042 Pozzoli, L., I. Bey, S. Rast, M. G. Schultz, P. Stier, and J. Feichter (2008), Trace gas and
1043 aerosol interactions in the fully coupled model of aerosol-chemistry-climate ECHAM5-
1044 HAMMOZ: 2. Impact of heterogeneous chemistry on the global aerosol distributions, *J.*
1045 *Geophys. Res*., 113, D07309, doi:10.1029/2007JD009008.

1046 Pozzoli, L., Janssens-Maenhout, G., Diehl, T., Bey, I., Schultz, M. G., Feichter, J.,
1047 Vignati, E., and Dentener, F. (2011), Re-analysis of tropospheric sulfate aerosol and
1048 ozone for the period 1980–2005 using the aerosol-chemistry-climate model ECHAM5-
1049 HAMMOZ, *Atmos. Chem. Phys*., 11, 9563-9594, doi:10.5194/acp-11-9563-2011.

1050 Prospero, J. M., P. Ginoux, O. Torres, S. E. Nicholson, and T. E. Gill (2002),
1051 Environmental characterization of global sources of atmospheric soil dust identified with

1052 the Nimbus 7 Total Ozone Mapping Spectrometer (TOMS) absorbing aerosol product,
1053 Rev. Geophys., 40(1), 1002, doi:10.1029/2000RG000095.

1054 Pu, B. and Ginoux, P. (2016), The impact of the Pacific Decadal Oscillation on
1055 springtime dust activity in Syria. *Atmos Chem Phys* **16**, 13431–13448, doi:10.5194/acp-
1056 16-13431-2016.

1057 Randles, C. A., and Coauthors, (2017), The MERRA-2 aerosol reanalysis, 1980 onward.
1058 Part I: System description and data assimilation evaluation. *J. Climate*, 30, 6823–
1059 6850, https://doi.org/10.1175/JCLI-D-16-0609.1.

1060 Redemann, J., M. A. Vaughan,Q. Zhang, Y. Shinozuka, P. B. Russell, J. M. Livingston,
1061 M. Kacenelenbogen, and L. A. Remer (2012), The comparison of MODIS-Aqua (C5) and
1062 CALIOP (V2 & V3) aerosol optical depth, Atmos. Chem. Phys., 12, 3025–3043,
1063 doi:10.5194/acp-12-3025-2012.

1064 Schulz, M., et al. (2006), Radiative forcing by aerosols as derived from the AeroCom
1065 present-day and pre-industrial simulations, *Atmos. Chem. Phys.*, 6, 5225– 5246.

1066 Shao, Y., K.-H. Wyrwoll, A. Chappell, J. Huang, Z. Lin, G. H. McTainsh, M. Mikami, T.
1067 Y. Tanaka, X. Wang, and S. Yoon (2011), Dust cycle: An emerging core theme in Earth
1068 system science, *Aeolian Res.*, **2**(4), 181–204, doi:10.1016/j.aeolia.2011.02.001.

1069 Song, Q., Z. Zhang, H. Yu, S. Kato, P. Yang, P. Colarco, L. A. Remer, C. L. Ryder, Net
1070 radiative effects of dust in tropical North Atlantic based on integrated satellite
1071 observations and in situ measurements, *Atmospheric Chemistry and Physics, 18,* 11303-
1072 11322, 2018.

1073 Stier, P., et al. (2005), The aerosol-climate model ECHAM5-HAM, *Atmos. Chem. Phys.*,
1074 5, 1125–1156.

1075 Su, L. and O. B. Toon (2011), Saharan and Asian dust: Similarities and differences
1076 determined by CALIPSO, AERONET, and a coupled climate-aerosol microphysical
1077 model, Atmos. Chem. Phys., 11, 3263-3280. doi:10.5194/acp-11-3263-2011.

1078 Tackett, J. L., D. M. Winker, B. J. Getzewich, M. A. Vaughan, S. A. Young, and J. Kar
1079 (2018), CALIPSO lidar level 3 aerosol profile product: version 3 algorithm design,
1080 Atmos. Meas. Tech., 11, 4129-4152, https://doi.org/10.5194/amt-11-4129-2018.

1081 Takemura, T., H. Okamoto, Y. Maruyama, A. Numaguti, A. Higurashi, and T. Nakajima
1082 (2000), Global three-dimensional simulation of aerosol optical thickness distribution of
1083 various origins, *J. Geophys. Res.*, 105, 17,853 – 17,873.

1084 Takemura, T., T. Nozawa, S. Emori, T. Y. Nakajima, and T. Nakajima (2005),
1085 Simulation of climate response to aerosol direct and indirect effects with aerosol
1086 transport-radiation model, *J. Geophys. Res.*, 110, D02202, doi:10.1029/2004JD005029.

1087 Tegen, I., S. P. Harrison, K. Kohfeld, I. C. Prentice, M. Coe, and M. Heimann (2002),
1088 Impact of vegetation and preferential source areas on global dust aerosol: Results from a
1089 model study, J. Geophys. Res., 107(D21), 4576, doi:10.1029/2001JD000963.

1090 Textor, C., et al. (2006), Analysis and quantification of the diversities of aerosol life
1091 cycles within AeroCom, *Atmos. Chem. Phys.*, *6*, 1777–1813.

Tesche, M., Ansmann, A. Müller, D., Althausen, D., Engelmann, R., Freudenthaler, V., and Groß S. (2009), Vertically resolved separation of dust and smoke over Cape Verde using multiwavelength Raman and polarization lidars during Saharan Mineral Dust Experiment 2008, J. Geophys. Res., 114, D13202, doi:10.1029/2009JD011862.

Uno, I., et al. (2006), Dust model intercomparison (DMIP) study over Asia: Overview, J. Geophys. Res., 111, D12213,doi:10.1029/2005JD006575.

Uno, I., Eguchi, K., Yumimoto, K., Takemura, T., Shimizu, A., Uematsu, M., Liu, Z., Wang, Z., Hara, Y., Sugimoto, N. (2009), Asian dust transported one fullcircuit around the globe. *Nat. Geosci*. 2, 557–560. http://dx.doi.org/10.1038/ngeo583.

Watson-Parris, D., N. Schutgens, D. Winker, S. P. Burton, R. A. Ferrare, and P. Stier (2018). On the limits of CALIOP for constraining modeled free tropospheric aerosol. *Geophysical Research Letters*, *45*. https://doi.org/10.1029/2018GL078195.

Wesely, M. L. (1989), Parameterization of surface resistance to gaseous dry deposition in regional-scale numerical models. Atmos. Environ., 23, 1293–1304.

Winker, D., Vaughan, M. A., Omar, A., Hu, Y. X., Powell, K. A., Liu, Z. Y., et al. (2009), Overview of the CALIPSO mission and CALIOP data processing algorithms. Journal of Atmospheric and Oceanic Technology, 26(11), 2310–2323.

Winker, D. M., Tackett, J. L., Getzewich, B. J., Liu, Z., Vaughan, M. A., & Rogers, R. R. (2013). The global 3-D distribution of tropospheric aerosols as characterized by CALIOP. Atmospheric Chemistry and Physics, 13(6), 3345–3361. https://doi.org/10.5194/acp-13-3345-2013.

Woodward, S. (2001), Modeling the atmospheric life cycle and radiative impact of mineral dust in the Hadley Centre climate model, J. Geophys. Res., 106, 18,155–18,166.

Wu, M., X. Liu, K. Yang, T. Luo, Z. Wang, C. Wu, K. Zhang, H. Yu, A. Darmenov (2019), Modeling dust in East Asia by CESM and sources of biases, *Journal of Geophysical Research - Atmospheres, 124,* 8043-8064, https://doi.org/10.1029/2019JD030799.

Young, S. A., M. A.Vaughan, A. Garnier, J. L. Tackett, J. B. Lambeth, and K. A. Powell (2018), Extinction and Optical Depth Retrievals for CALIPSO's Version 4 Data Release, Atmos. Meas. Tech. Discuss., https://doi.org/10.5194/amt-2018-182, in review.

Yu, H., L. A. Remer, M. Chin, H. Bian, R. Kleidman, and T. Diehl (2008), A satellite-based assessment of trans-Pacific transport of pollution aerosol, *Journal of Geophysical Research - Atmospheres, 113,* D14S12, doi:10.1029/2007JD009349.

Yu, H., M. Chin, L. A. Remer, R. G. Kleidman, N. Bellouin, H. Bian, and T. Diehl (2009), Variability of marine aerosol fine-mode fraction and estimates of anthropogenic aerosol component over cloud-free oceans from the Moderate Resolution Imaging Spectroradiometer (MODIS), *J. Geophys. Res*., 114, D10206, doi:10.1029/2008JD010648.

Yu, H., M. Chin, D. M. Winker, A. H. Omar, Z. Liu, C. Kittaka, and T. Diehl (2010), Global view of aerosol vertical distributions from CALIPSO lidar measurements and GOCART simulations: Regional and seasonal variations, J. Geophys. Res., 115,

D00H30, doi:10.1029/2009JD013364.

Yu, H., L. Remer, M. Chin, H. Bian, Q. Tan, T. Yuan, and Y. Zhang (2012), Aerosols from Overseas Rival Domestic Emissions over North America. *Science*, *337*, 566-569. doi:10.1126/science.1217576.

Yu, H., L. A. Remer, R. A. Kahn, M. Chin, and Y. Zhang (2013), Satellite perspective of aerosol intercontinental transport: from qualitative tracking to quantitative characterization, Atmos. Res., 124, 73-100, 2013.

Yu, H., M. Chin, T. Yuan, H. Bian, L. A. Remer, J. M. Prospero, A. Omar, D. Winker, Y. Yang, Y. Zhang, Z. Zhang, and C. Zhao (2015a), The fertilizing role of African dust in the Amazon rainforest: A first multiyear assessment based on data from Cloud-Aerosol Lidar and Infrared Pathfinder Satellite Observations, Geophys. Res. Lett., 42, doi:10.1002/2015GL06304.

Yu, H., et al. (2015b), Quantification of trans-Atlantic dust transport from seven-year (2007–2013) record of CALIPSO lidar measurements, Remote Sens. Environ., 159, 232–249., http://dx.doi.org/10.1016/j.rse.2014.12.010.

Yu, H., Q. Tan, M. Chin, L. A. Remer, R. A. Kahn, H. Bian, D. Kim, Z. Zhang, T. Yuan, A. H. Omar, D. M. Winker, R. C. Ley, O. Kalashnikova, L. Crepeau, V. Capelle, A. Chedin (2019a), Estimates of African dust deposition along the trans-Atlantic transit using the decadelong record of aerosol measurements from CALIOP, MODIS, MISR, and IASI. *Journal of Geophysical Research – Atmospheres, 124,* 7975-7996, https://doi.org/10.1029/2019JD030574.

Yu, H., Y. Yang, H. Wang, Q. Tan, M. Chin, R. Levy, L.A. Remer, S.J. Smith, T. Yuan, Y. Shi (2019b), Interannual Variability and Trends of Combustion Aerosol and Dust in Major Continental Outflows Revealed by MODIS Retrievals and CAM5 Simulations During 2003 – 2017, *Atmospheric Chemistry and Physics Discussion, https://doi.org/10.5194/acp-2019-621,* 2019.

Zhao, T. L., S. L. Gong, X. Y. Zhang, J.-P. Blanchet, I. G. McKendry, and Z. J. Zhou (2006), A simulated climatology of Asian dust aerosol and its trans-pacific transport. Part I: Mean climate and validation, *J. Clim.*, **19**, 88–103, doi:10.1175/JCLI3605.1.

Table 1. Description of the participating models and their physical characteristics of dust. Adopted from Kim et al. (2014).

	GOCART (GO)	GISS-E2-OMA (GI)	SPRINTARS (SP)	ECHAM5-HAMMOZ* (EC)	HadGEM2 (HG)
Resolution	2.5°×2°	2.5°×2°	1.125°×1.125°	2.8°×2.8°	1.875°×1.25°
Vertical Layers	30	40	56	31	38
Meteorology	GEOS-4 DAS	Horizontal winds nudged to NCEP Reanalysis	NCEP Reanalysis	ECMWF Reanalysis	ECMWF Reanalysis
Winds for emissions	U_{10m}^3	U_{10m}^3	U_{10m}^3	U_*^3	U_*^3
Size distribution (μm)	5 bins 0.1-1.0-1.8-3.0-6.0-10.0	5 bins 0.1-1-2-4-8-16	6 bins 0.1-0.22-0.46-1.0-2.15-4.64-10.0	2 modes (acc. And coarse) $0.05<r_m<0.5$ $0.5<r_m$	6 bins 0.0316-0.1-0.316-1.0-3.16-10-31.6
Density (g cm^{-3})	2.5	2.5 for clay 2.65 for silt	2.6	2.5-2.6	2.65
Dust-related key references	Chin et al. (2002,2009) Ginoux et al. (2001)	Miller et al., (2006); Bauer and Koch (2005)	Takemura et al. (2000, 2005)	Pozzoli et al. (2008, 2011)	Bellouin et al. (2011) (Appendix A)

* Dust particles are emitted in the insoluble accumulation and coarse modes with mass median radii of 0.37 μm and 1.75 μm, respectively. Once emitted dust particles can be mixed with other aerosols, and dust is distributed in two additional modes, internally mixed soluble accumulation and coarse modes.

1171

1172 Table 2: Remote sensing data used in this study. Adopted from Kim et al. (2014).

Sensor/platform	Data products	Major references
MODIS	AOD (combined dark target and deep blue)	Levy et al. (2013); Hsu et al. (2004)
	DOD derived from AOD and aerosol fine-mode fraction over ocean	Kaufman et al. (2005); Yu et al. (2009, 2019b)
	DOD derived from deep blue retrievals over land	Ginoux et al. (2012); Pu and Ginoux (2016)
CALIOP	Aerosol and dust extinction profiles	Winker et al. (2009); Young et al. (2018); Yu et al. (2012, 2015b, 2019a)
MISR	AOD, non-spherical AOD	Kalashnikova and Kahn (2006); Kahn et al. (2010)
AERONET	AOD, coarse-mode AOD	Holben et al. (1998); Dubovik et al. (2000)

1173

Table 3. Mean of optical properties of satellite over land and ocean domains. f_{DOD} is the ratio of DOD to AOD. Data is not available over land for some sensors. [1]Mean of satellites.

	Name	Unit	MODIS	MISR	CALIOP	Mean[1]
Domain (60°E-140°W, 20°N-60°N)	AOD	Unitless	0.226	0.194	0.152	0.191
	DOD	Unitless	0.085	-	0.061	0.073
	f_{DOD}	Fraction	0.329	-	0.352	0.341
Land (60°E-140°E, 20°N-60°N)	AOD	Unitless	0.274	0.209	0.217	0.233
	DOD	Unitless	0.111	-	0.094	0.103
	f_{DOD}	Fraction	0.362	-	0.416	0.389
Ocean (140°E-140°W, 20°N-60°N)	AOD	Unitless	0.177	0.179	0.084	0.147
	DOD	Unitless	0.059	0.054	0.027	0.047
	f_{DOD}	Fraction	0.296	0.268	0.285	0.283

Table 4. Budget analysis and optical properties of dust over different domains. Listed parameters are emission (EMI), dry deposition (DRY), wet deposition (WET), column mass loading (LOAD), aerosol optical depth (AOD), dust optical depth (DOD), DOD fraction to AOD (f_{DOD}), WET fraction to total deposition (f_{WET}), loss frequency (LF), mass extinction efficiency (MEE). Diversity of model parameters (%) is defined as the ratio of standard deviation to the mean of a parameter following Textor et al. (2006). Clear-sky AOD is listed for GISS.

	Name	Unit	GOCART	GISS	SPRINTARS	ECHAM5	HadGEM2	Model mean	Diversity (%)
Domain (60°E-140°W, 20°N-60°N)	EMI	Tg yr^{-1}	680.5	200.4	825.9	77.4	488.8	454.6	69.3
	DRY	Tg yr^{-1}	518.8	123.4	468.0	35.1	323.5	293.8	71.8
	WET	Tg yr^{-1}	164.4	105.8	150.8	70.0	73.2	112.8	38.5
	LOAD	Tg	9.12	2.35	3.06	0.75	1.45	3.34	100.0
	AOD	Unitless	0.202	0.191	0.157	0.182	0.166	0.180	10.2
	DOD	Unitless	0.080	0.028	0.045	0.008	0.013	0.035	83.6
	f_{DOD}	Fraction	0.352	0.138	0.234	0.058	0.101	0.177	66.6
	f_{WET}	Fraction	0.50	0.76	0.62	0.66	0.79	0.66	17.4
	LF	day^{-1}	0.15	0.23	0.26	0.37	0.25	0.25	31.0
	MEE	m^2g^{-1}	0.59	0.79	1.06	0.67	0.77	0.78	23.0
Land (60°E-140°E, 20°N-60°N)	DRY	Tg yr^{-1}	495.1	121.5	464.6	33.8	323.0	287.60	71.2
	WET	Tg yr^{-1}	123.2	89.1	134.9	64.3	66.0	95.50	33.9
	LOAD	Tg	6.60	2.05	2.67	0.69	1.22	2.64	88.4
	AOD	Unitless	0.249	0.193	0.202	0.182	0.197	0.205	12.7
	DOD	Unitless	0.111	0.048	0.075	0.014	0.020	0.054	75.1
	f_{DOD}	Fraction	0.416	0.226	0.345	0.110	0.153	0.250	51.4
	f_{WET}	Fraction	0.38	0.62	0.51	0.57	0.67	0.55	20.0
	LF	day^{-1}	0.20	0.28	0.39	0.53	0.41	0.36	35.3
	MEE	m^2g^{-1}	0.57	0.71	1.01	0.66	0.68	0.73	23.0
Ocean (140°E-140°W, 20°N-60°N)	DRY	Tg yr^{-1}	25.0	1.9	3.4	1.3	0.5	6.4	162.6
	WET	Tg yr^{-1}	43.3	16.7	15.9	5.7	7.2	17.8	85.1
	LOAD	Tg	2.62	0.30	0.39	0.06	0.23	0.72	148.4
	AOD	Unitless	0.155	0.189	0.111	0.182	0.136	0.155	20.9
	DOD	Unitless	0.049	0.009	0.014	0.001	0.006	0.016	121.2
	f_{DOD}	Fraction	0.286	0.049	0.122	0.007	0.048	0.102	108.1
	f_{WET}	Fraction	0.62	0.89	0.73	0.74	0.92	0.78	15.8
	LF	day^{-1}	0.10	0.18	0.13	0.21	0.09	0.14	34.5
	MEE	m^2g^{-1}	0.61	0.86	1.12	0.68	0.86	0.83	23.8

Table 5. Multi-model mean and diversity over land and ocean domains for North Africa and Asia. The values of North Africa are adopted from Kim et al. (2014). Numbers in parenthesis are the diversity of model parameters (%), which is defined as the ratio of standard deviation to the mean of a parameter following Textor et al. (2006).

Name	Unit	Land		Ocean	
		North Africa (17°W-30°E, 0°N-35°N)	Asia (60°E-140°E, 20°N-60°N)	North Africa (90°W-17°W, 0°N-35°N)	Asia (140°E-140°W, 20°N-60°N)
EMI	Tg yr^{-1}	1047.8 (57.1)	454.6 (69.3)	-	-
LOAD	Tg yr^{-1}	5.78 (74.8)	2.64 (88.4)	2.46 (56.5)	0.72 (148.4)
AOD	Unitless	0.29 (50.3)	0.21 (12.7)	0.17 (33.6)	0.16 (20.9)
DOD	Unitless	0.18 (65.8)	0.05 (75.1)	0.06 (44.8)	0.02 (121.2)
f_{DOD}	Fraction	0.52 (31.1)	0.25 (51.4)	0.23 (50.2)	0.10 (108.1)
f_{WET}	Fraction	0.32 (15.3)	0.55 (20.0)	0.62 (23.4)	0.78 (15.8)
LF	day^{-1}	0.39 (44.0)	0.36 (35.3)	0.29 (37.1)	0.14 (34.5)
MEE	m^2g^{-1}	0.65 (26.9)	0.73 (23.0)	0.76 (29.3)	0.83 (23.8)

Table 6. Mean of AOD, DOD and f_{DOD} of CALIOP satellite over land and ocean domains with different integration options of CAD score and clear-sky.

Cases	Land			Ocean		
	AOD	DOD	f_{DOD}	AOD	DOD	f_{DOD}
-100<CAD<-20, exclude clear-air	0.416	0.197	0.429	0.205	0.079	0.305
-100<CAD<-20, include clear-air	0.223	0.109	0.425	0.117	0.040	0.291
-100<CAD<-70, exclude clear-air	0.388	0.169	0.410	0.178	0.058	0.286
-100<CAD<-70, include clear-air	0.211	0.095	0.409	0.104	0.032	0.274

Figure Captions

Figure 1. Name and location of the sub-domains for (1) climatology (black dash-boxes) and (2) CALIOP (red boxes) analysis. Color map is the annual mean of CALIOP DOD. Color circles superimposed on the map are the AERONET retrieved coarse mode AOD. The domains for climatological analysis are LAND [60°E-140°E; 20°N-60°N] and OCEAN [140°E-140°W; 20°N-60°N]. The domain for CALIOP analysis are THAR [70°E-75°E; 25°N-30°N], TAKL [75°E-90°E; 35°N-45°N], GOBI [95°E-115°E; 40°N-45°N], NWP [135°E-140°E; 25°N-50°N], NCP [175°E-180°E; 30°N-55°N], and NEP [130°W-125°W; 35°N-60°N].

Figure 2. Spatial distribution of mean AOD from satellites (MODIS, MISR, and CALIOP) and models (GOCART, GISS, SPRINTARS, ECHAM5, and HadGEM2) averaged over 2000-2005. CALIOP including clear-air samples is averaged for 2007-2011. Color circles superimposed on the map represent AERONET observed AOD.

Figure 3. Spatial distribution of mean dust optical depth (DOD) from satellites (MODIS, MISR, and CALIOP) and models (GOCART, GISS, SPRINTARS, ECHAM5, and HadGEM2) averaged over 2000-2005. CALIOP including clear-air samples and is averaged for 2007-2011. Color circles superimposed on the map are the AERONET retrieved coarse mode AOD.

Figure 4. (a) Meridional mean of AOD, DOD, and f_{DOD} averaged from 20°N to 60°N. Thick lines are satellite retrievals from MODIS (MD), MISR (MI), and CALIOP (CA), and thin lines are model simulations. No DOD is available over land in MISR products. Asia and North America is shaded in gray. (b) Same as (a), except for normalized to values of each variable at the Asian coast of 130°E.

Figure 5. Monthly mean of (top) AOD, (middle) DOD, (bottom) f_{DOD} for land [60°E-140°E; 20°N-60°N]. Left- and right-columns are from satellites and model, respectively. All model plots are averaged from 2000 to 2005. Vertical bars are the standard deviation of monthly mean values.

Figure 6. Monthly mean of (top) AOD, (middle) DOD, (bottom) f_{DOD} for ocean [140°E-140°W; 20°N-60°N]. Left- and right-columns are from satellites and model, respectively. All model plots are averaged from 2000 to 2005. Vertical bars are the standard deviation of monthly mean values.

Figure 7. Mean spring season vertical profile of extinction coefficient of total aerosol (σ_{aer} in km^{-1}), extinction coefficient of dust (σ_{du} in km^{-1}), and $f\sigma_{du}$, the ratio of σ_{du} to σ_{aer} for THAR (Thar desert), TAKL (Taklimakan desert), and GOBI (Gobi desert) domains. Model simulations are for 2006. CALIOP data is averaged from 2007 to 2011. Black solid and dashed-lines are the means of CALIOP data including clear-air samples and excluding clear-air samples, respectively, representing the lower and upper limits for the CALIOP data (range shaded in grey). Numbers in parenthesis are CALIOP data excluding clear-air samples.

Figure 8. Same as Figure 7 except for (left) north-west Pacific domain, (middle) north-center Pacific, (right) north-east Pacific domains.

Figure 9. Mean dust emissions from models averaged from 2000 to 2005. Color contour unit is in $g km^{-2} s^{-1}$.

Figure 10. Map of loss frequency, f_{WET}, and MEE for dust from models averaged from 2000 to 2005. (a) Loss frequency is the ratio of total removal rate to LOAD (day^{-1}), (b) f_{WET} is the fraction of wet removal to the total removal, and (c) MEE is dust mass extinction efficiency at 550 nm ($m^2 g^{-1}$).

Figure 11. The partial sensitivity of DOD to various determining factors of Source (SRC = EMI + mass imbalance), residence time (RES), and mass extinction efficiency (MEE). Model values (GOCART, SPRINTARS, ECHAM5, HadGEM2, and GISS) are averaged for 2000-2005 over the domain (60°E-140°W, 20°N-60°N). "x" symbol of each model is the partial sensitivity of DOD to EMI within the domain. MO and CA are the mean DOD from MODIS and CALIOP averaged over the same time and domain, respectively.

Figure 12. Multi-model mean of optical and physical parameters over (a) Asia and North Africa and (b) Pacific ocean and Atlantic ocean. Models (GOCART, SPRINTARS, ECHAM5, HadGEM2, and GISS) are averaged from 2000 to 2005. Error bars are the standard deviation of model values.

Figure 13. (left) Spatial distribution of mean AOD, DOD, and f_{DOD} from CALIOP averaged for 2007-2011, where, CALIOP excludes clear-air samples. Color circles superimposed on the map represent AERONET data. (right) same as Figure 4a except for CALIOP excludes clear-air samples.

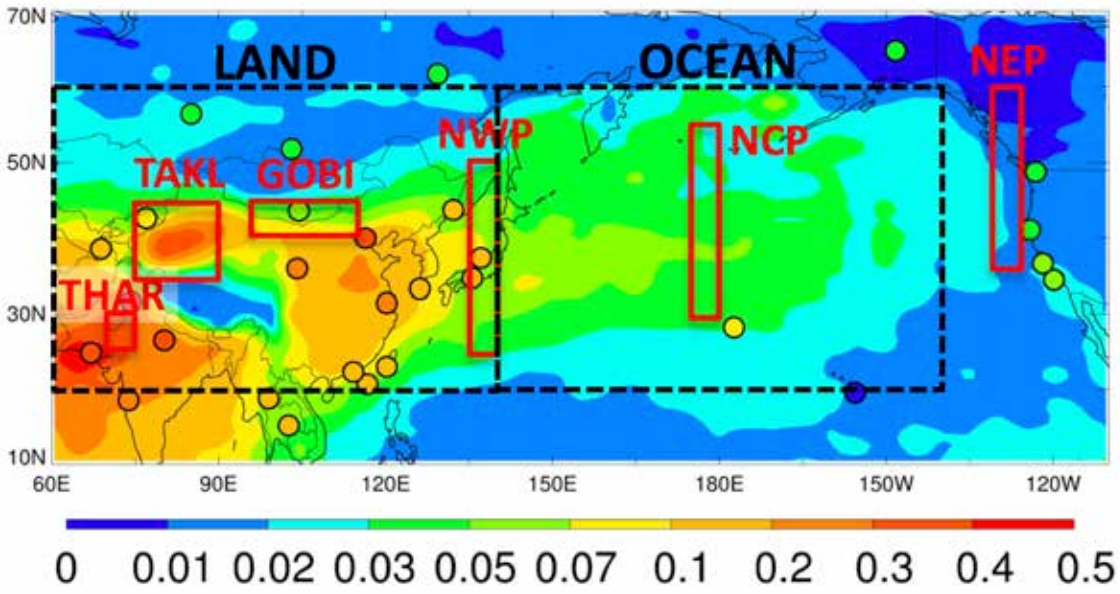

Figure 1. Name and location of the sub-domains for (1) climatology (black dash-boxes) and (2) CALIOP (red boxes) analysis. Color map is the annual mean of CALIOP DOD. Color circles superimposed on the map are the AERONET retrieved coarse mode AOD. The domain for climatological analysis are LAND [60°E-140°E; 20°N-60°N] and OCEAN [140°E-140°W; 20°N-60°N]. The domain for CALIOP analysis are THAR [70°E-75°E; 25°N-30°N], TAKL [75°E-90°E; 35°N-45°N], GOBI [95°E-115°E; 40°N-45°N], NWP [135°E-140°E; 25°N-50°N], NCP [175°E-180°E; 30°N-55°N], and NEP [130°W-125°W; 35°N-60°N].

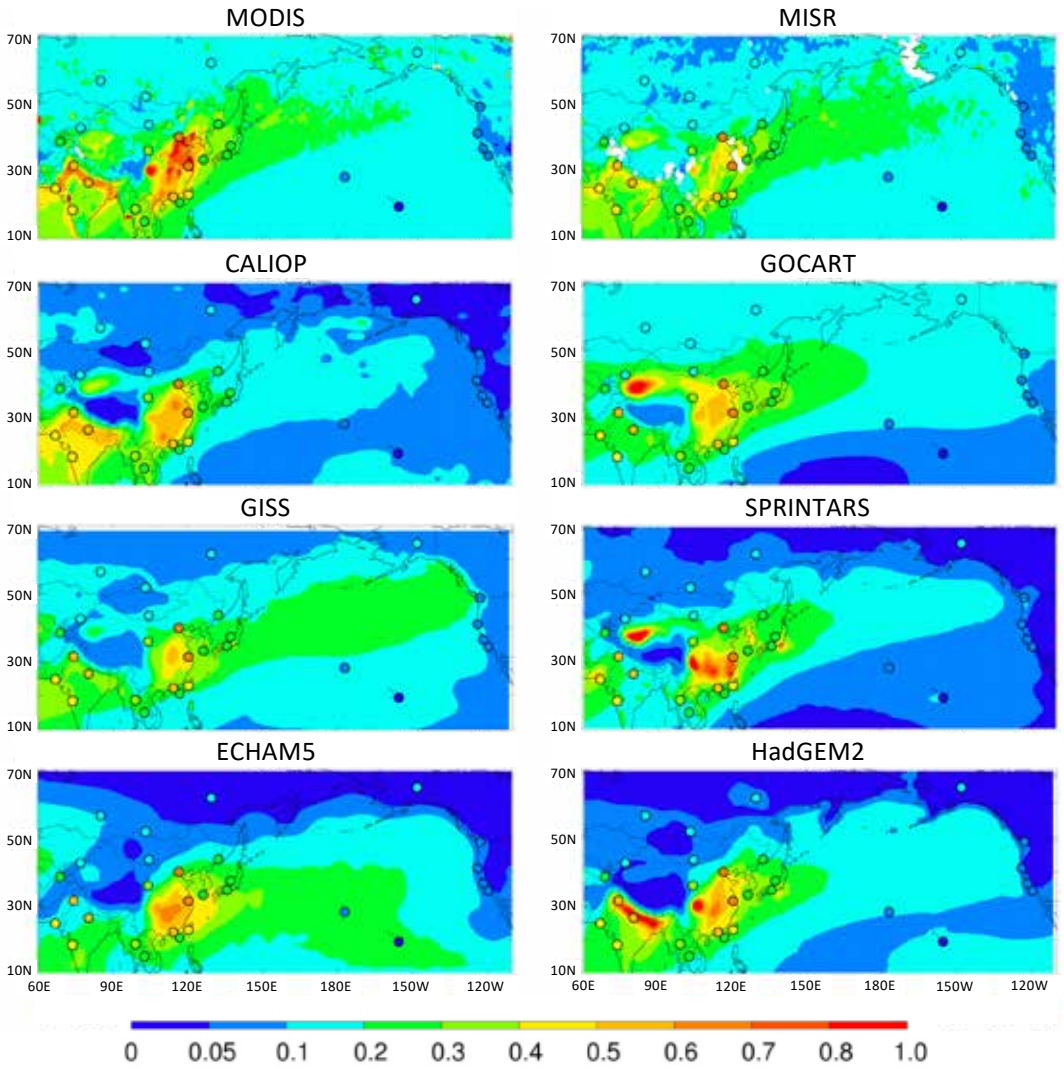

Figure 2. Spatial distribution of mean AOD from satellites (MODIS, MISR, and CALIOP) and models (GOCART, GISS, SPRINTARS, ECHAM5, and HadGEM2) averaged over 2000-2005. CALIOP including clear-air samples is averaged for 2007-2011. Color circles superimposed on the map represent AERONET observed AOD.

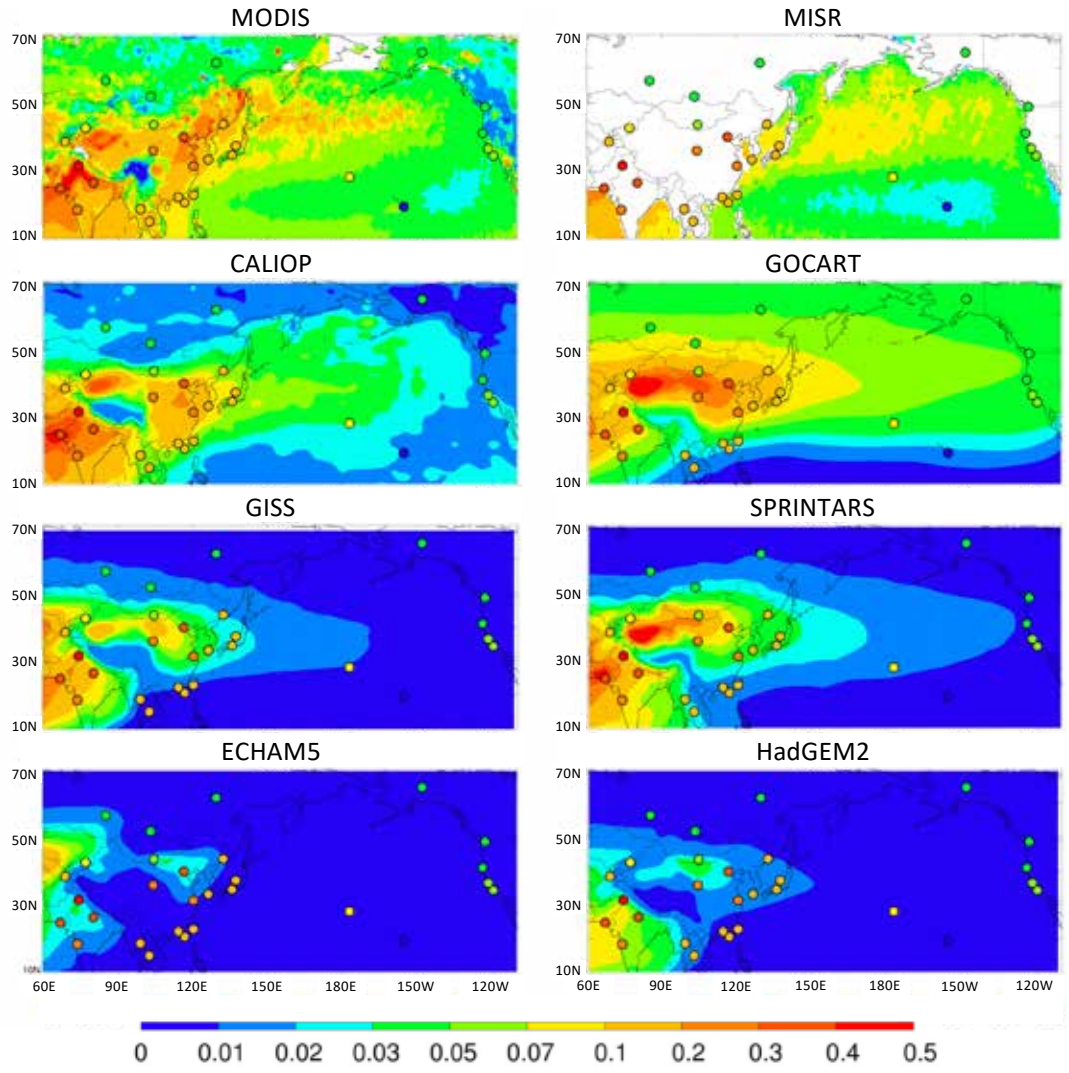

Figure 3. Spatial distribution of mean dust optical depth (DOD) from satellites (MODIS, MISR, and CALIOP) and models (GOCART, GISS, SPRINTARS, ECHAM5, and HadGEM2) averaged over 2000-2005. CALIOP including clear-air samples and is averaged for 2007-2011. Color circles superimposed on the map are the AERONET retrieved coarse mode AOD.

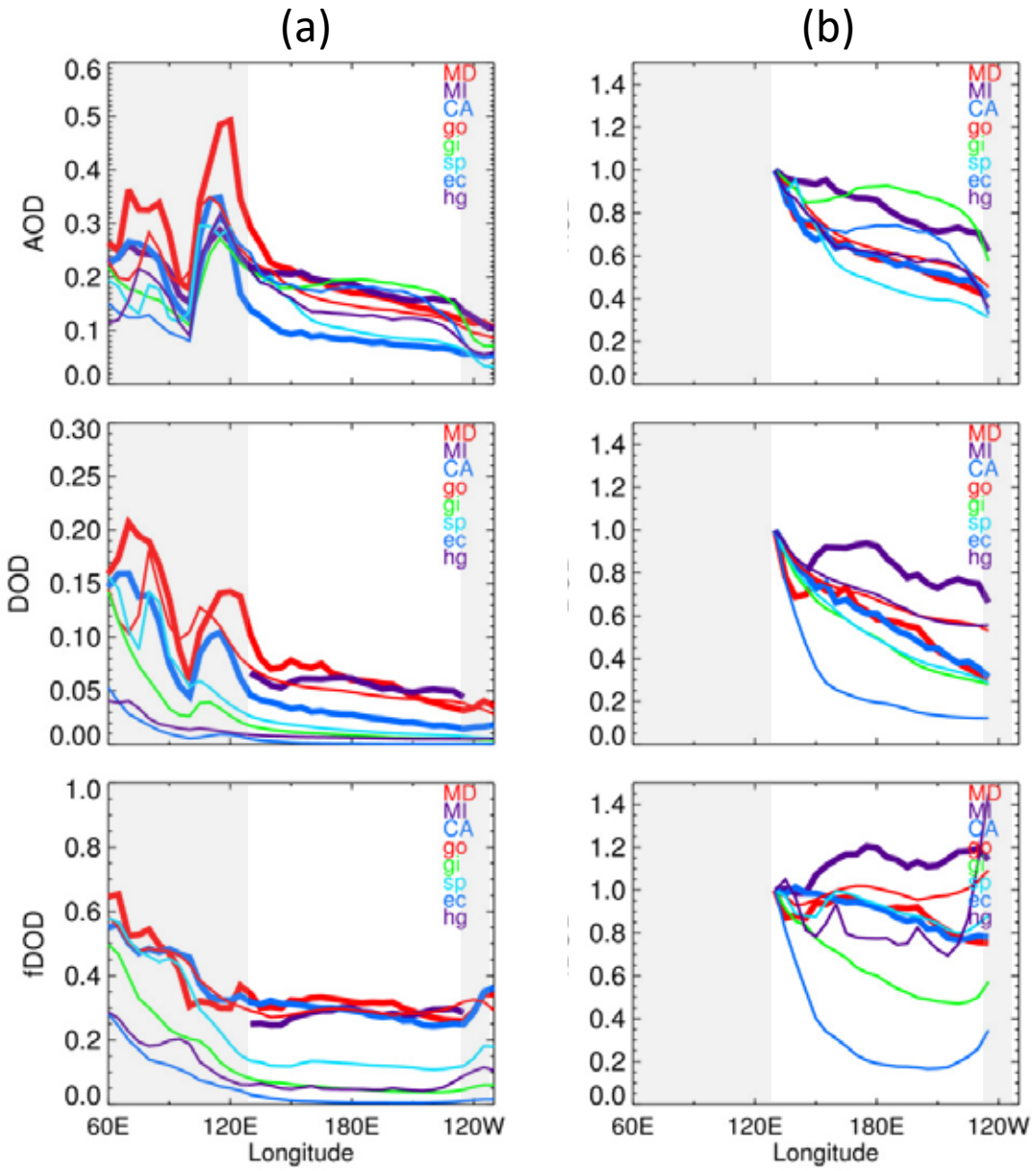

Figure 4. (a) Meridional mean of AOD, DOD, and f_{DOD} averaged from 20°N to 60°N. Thick lines are satellite retrievals from MODIS (MD), MISR (MI), and CALIOP (CA), and thin lines are model simulations. No DOD is available over land in MISR products. Asia and North America is shaded in gray. (b) Same as (a), except for normalized to values of each variable at the Asian coast of 130°E.

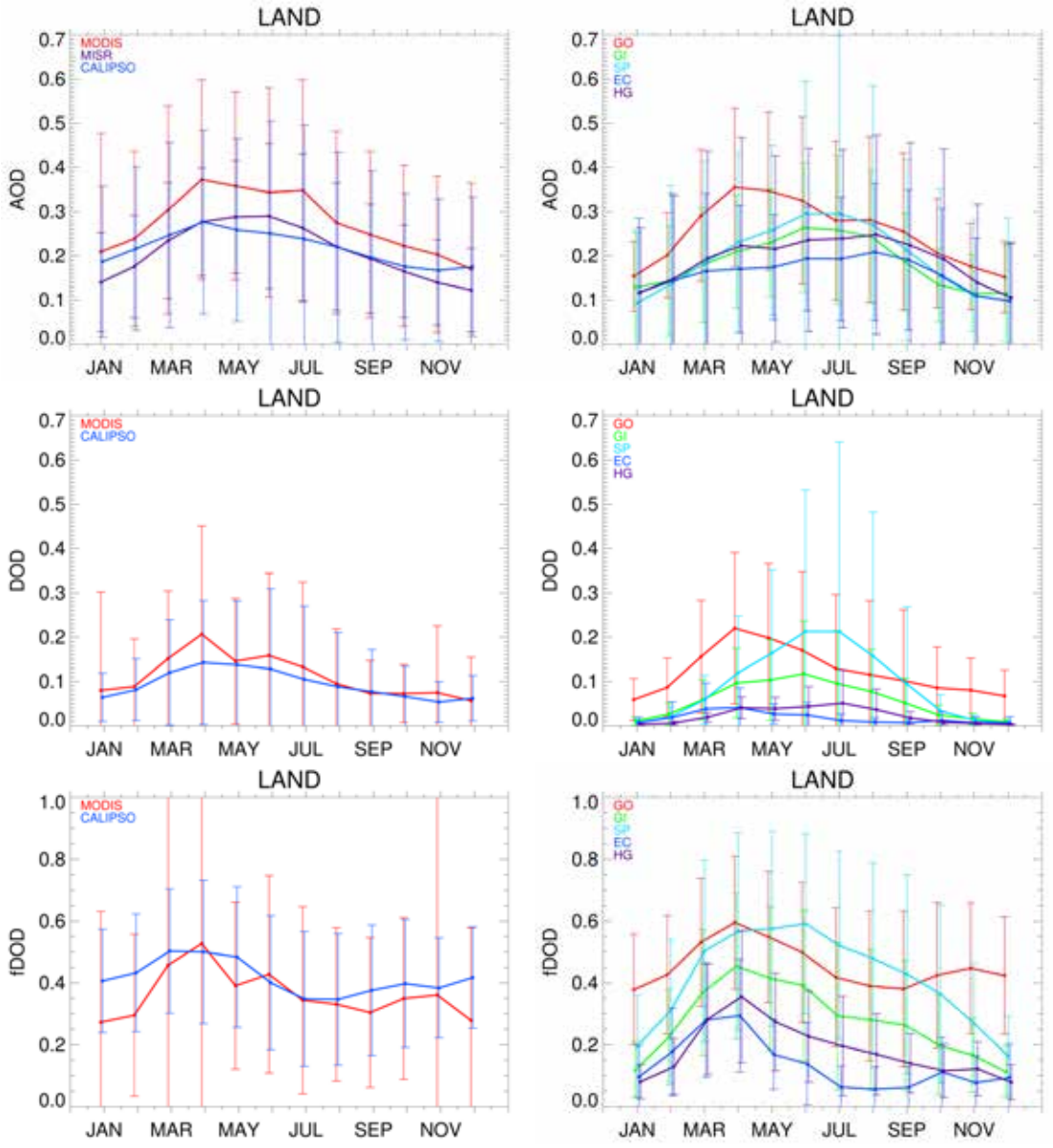

Figure 5. Monthly mean of (top) AOD, (middle) DOD, (bottom) f_{DOD} for land [60°E-140°E; 20°N-60°N]. Left- and right-columns are from satellites and model, respectively. All model plots are averaged from 2000 to 2005. Vertical bars are the standard deviation of monthly mean values.

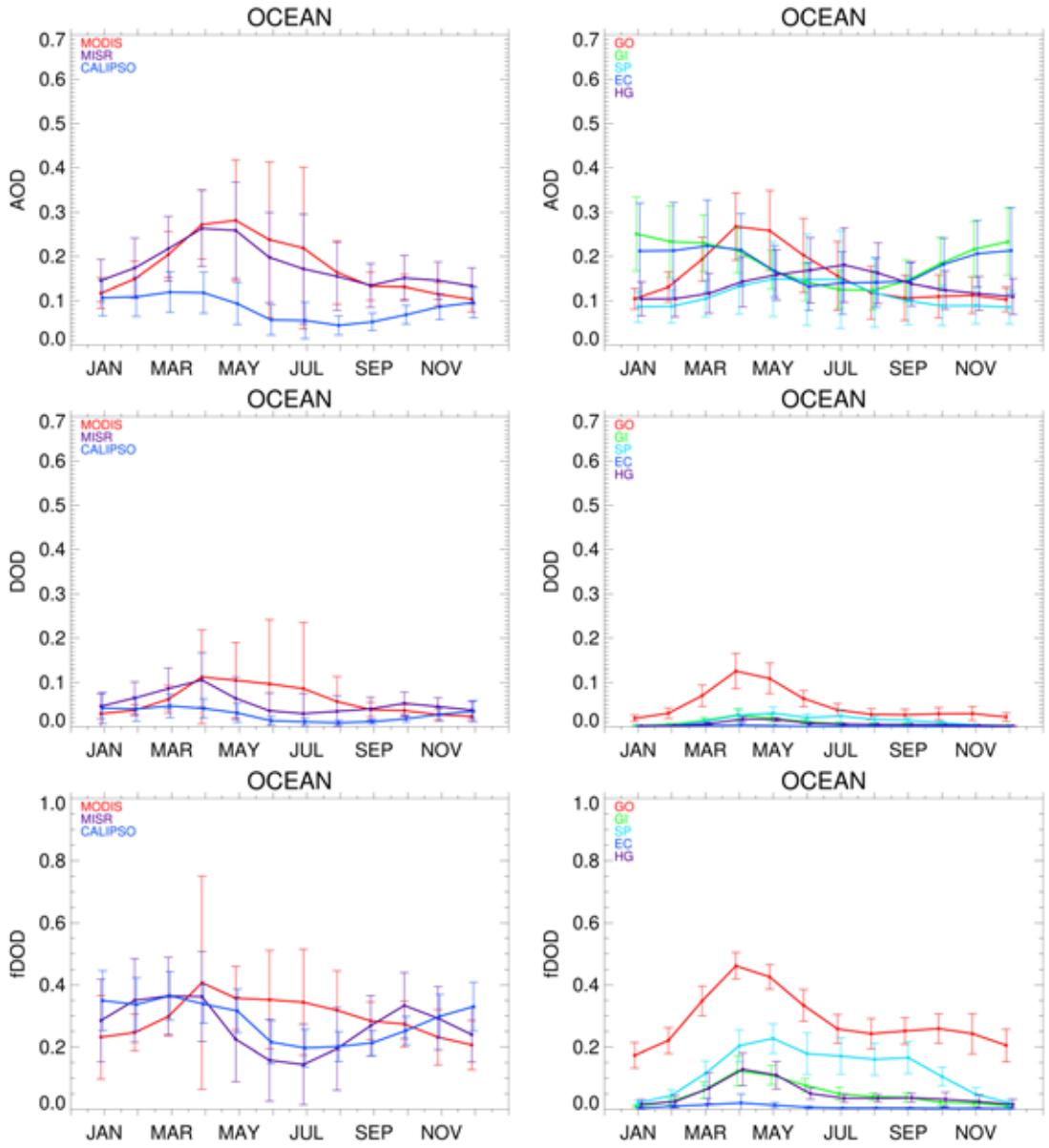

Figure 6. Monthly mean of (top) AOD, (middle) DOD, (bottom) f_{DOD} for ocean [140°E-140°W; 20°N-60°N]. Left- and right-columns are from satellites and model, respectively. All model plots are averaged from 2000 to 2005. Vertical bars are the standard deviation of monthly mean values.

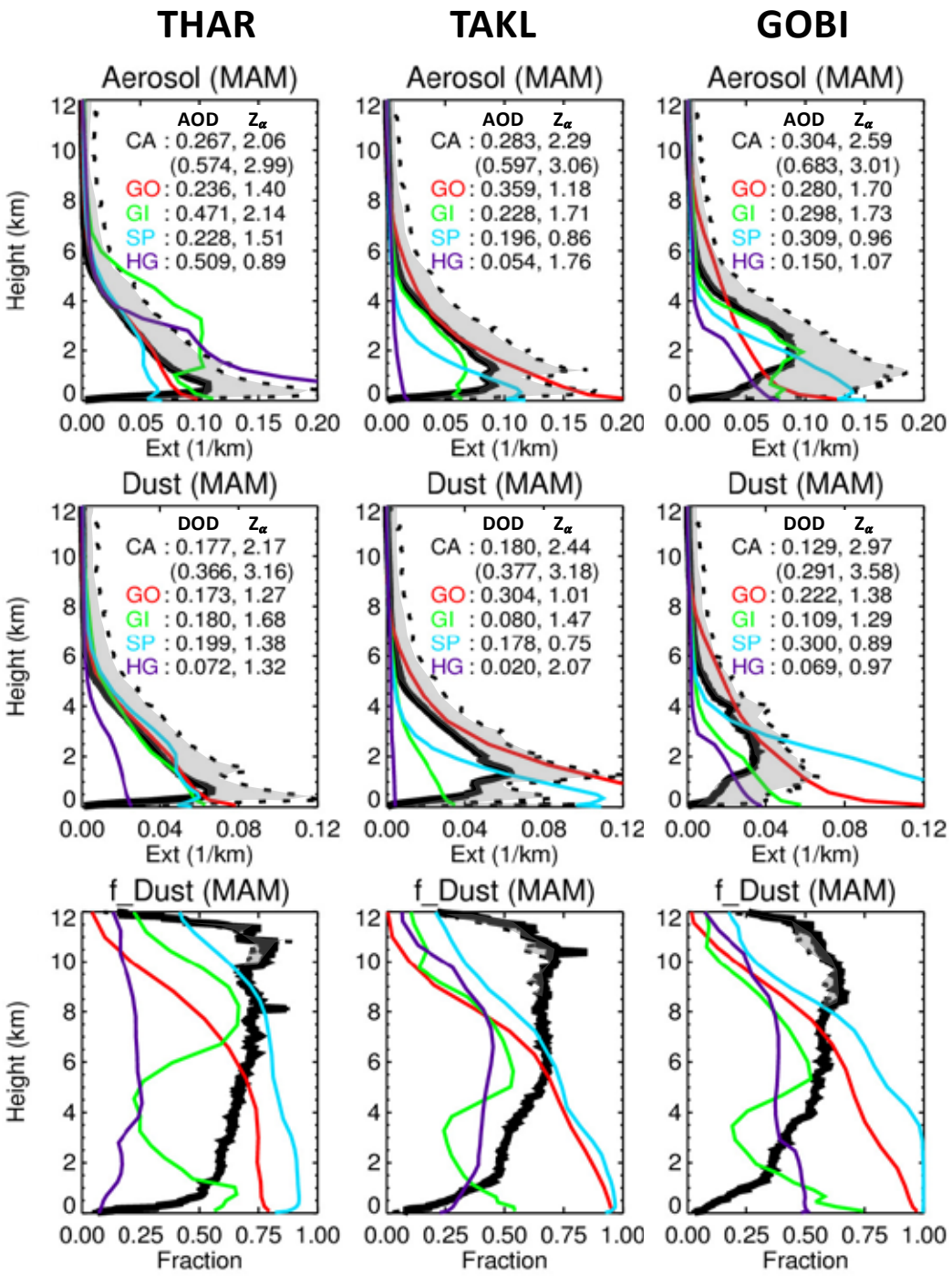

Figure 7. Mean spring season vertical profile of extinction coefficient of total aerosol (σ_{aer} in km^{-1}), extinction coefficient of dust (σ_{du} in km^{-1}), and $f\sigma_{du}$, the ratio of σ_{du} to σ_{aer} for THAR (Thar desert), TAKL (Taklimakan desert), and GOBI (Gobi desert) domains. Model simulations are for 2006. CALIOP data is averaged from 2007 to 2011. Black solid and dashed-lines are the means of CALIOP data including clear-air samples and excluding clear-air samples, respectively, representing the lower and upper limits for the

CALIOP data (range shaded in grey). Numbers in parenthesis are CALIOP data excluding clear-air samples.

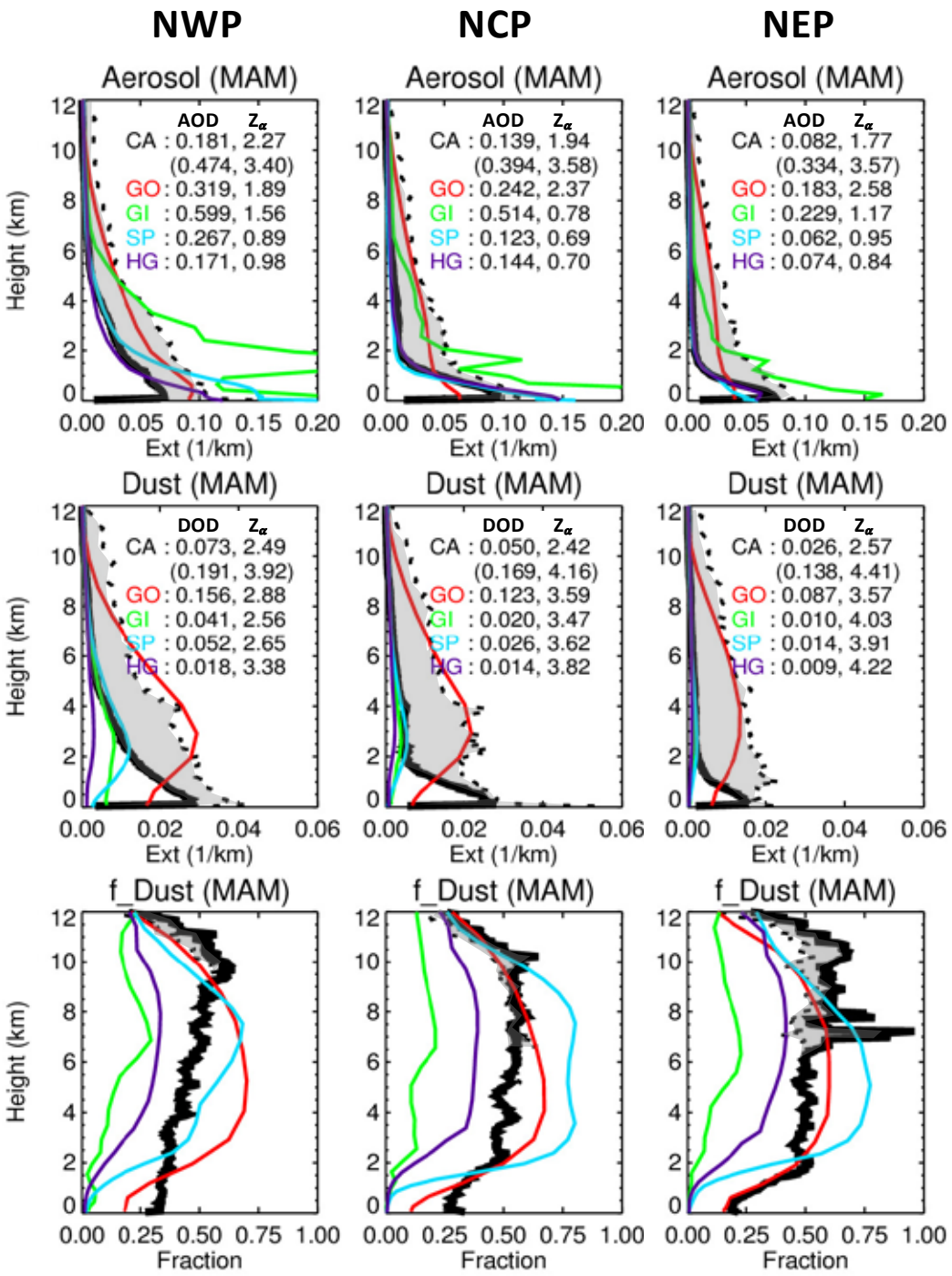

Figure 8. Same as Figure 7 except for (left) north-west Pacific domain, (middle) north-center Pacific, (right) north-east Pacific domains.

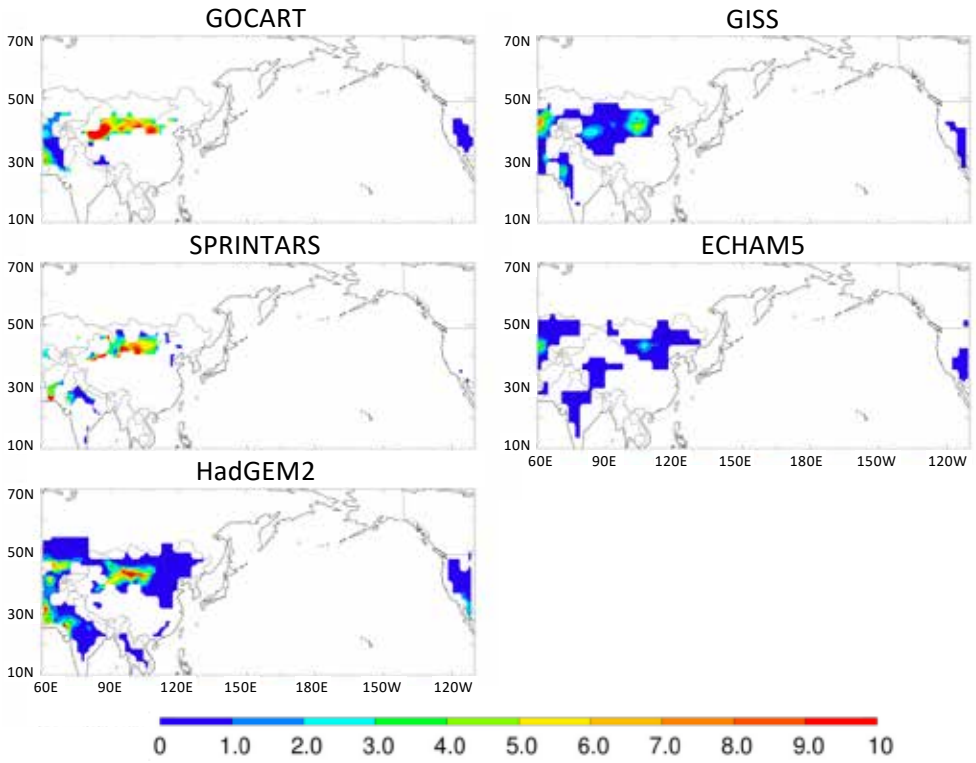

Figure 9. Mean dust emissions from models averaged from 2000 to 2005. Color contour unit is in $gkm^{-2}s^{-1}$.

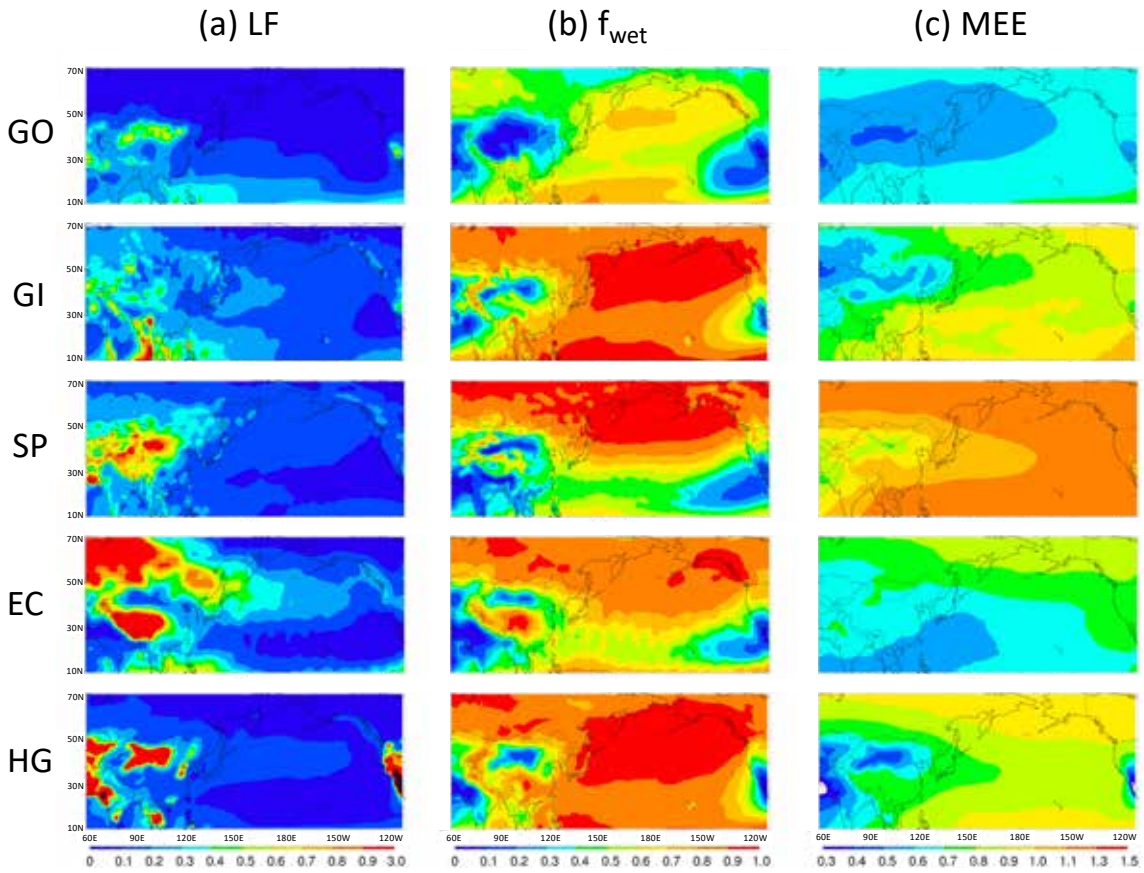

Figure 10. Map of loss frequency, f_{WET}, and MEE for dust from models averaged from 2000 to 2005. (a) Loss frequency is the ratio of total removal rate to LOAD (day^{-1}), (b) f_{WET} is the fraction of wet removal to the total removal, and (c) MEE is dust mass extinction efficiency at 550 nm (m^2g^{-1}).

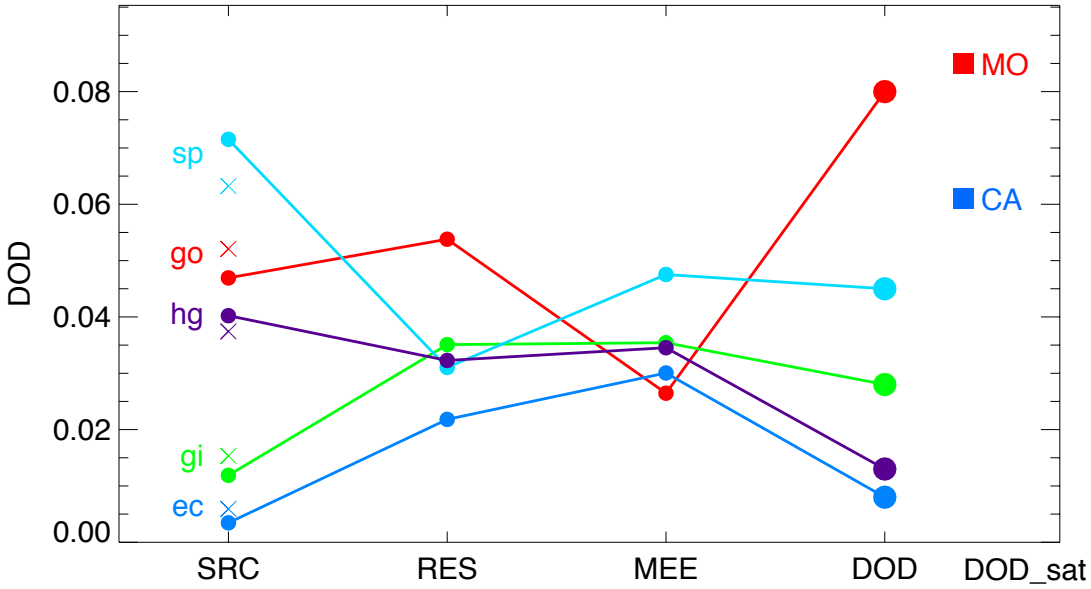

Figure 11. The partial sensitivity of DOD to various determining factors of Source (SRC = EMI + mass imbalance), residence time (RES), and mass extinction efficiency (MEE). Model values (GOCART, SPRINTARS, ECHAM5, HadGEM2, and GISS) are averaged for 2000-2005 over the domain (60°E-140°W, 20°N-60°N). "x" symbol of each model is the partial sensitivity of DOD to EMI within the domain. MO and CA are the mean DOD from MODIS and CALIOP averaged over the same time and domain, respectively.

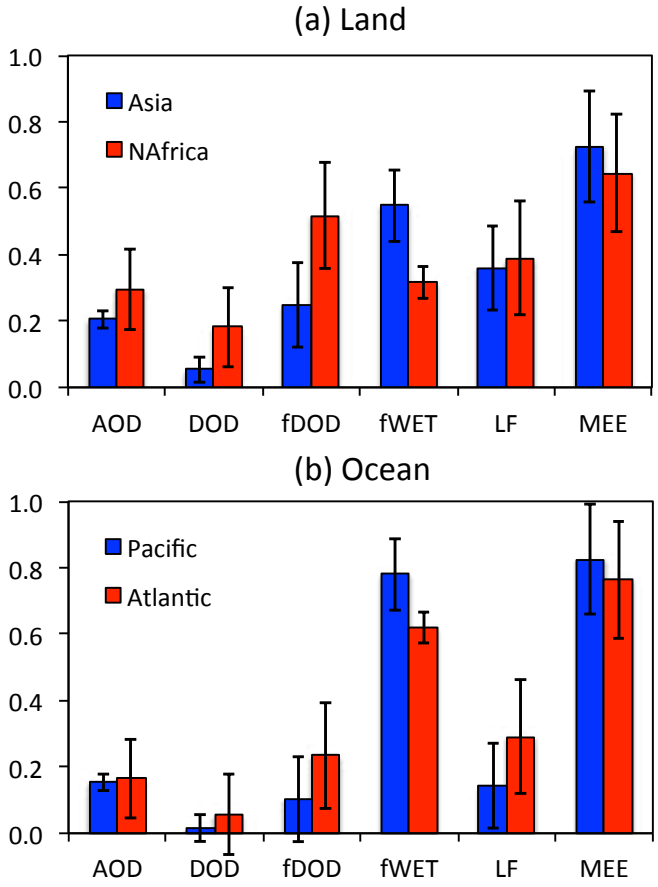

Figure 12. Multi-model mean of optical and physical parameters over (a) Asia and North Africa and (b) Pacific ocean and Atlantic ocean. Models (GOCART, SPRINTARS, ECHAM5, HadGEM2, and GISS) are averaged from 2000 to 2005. Error bars are the standard deviation of model values.

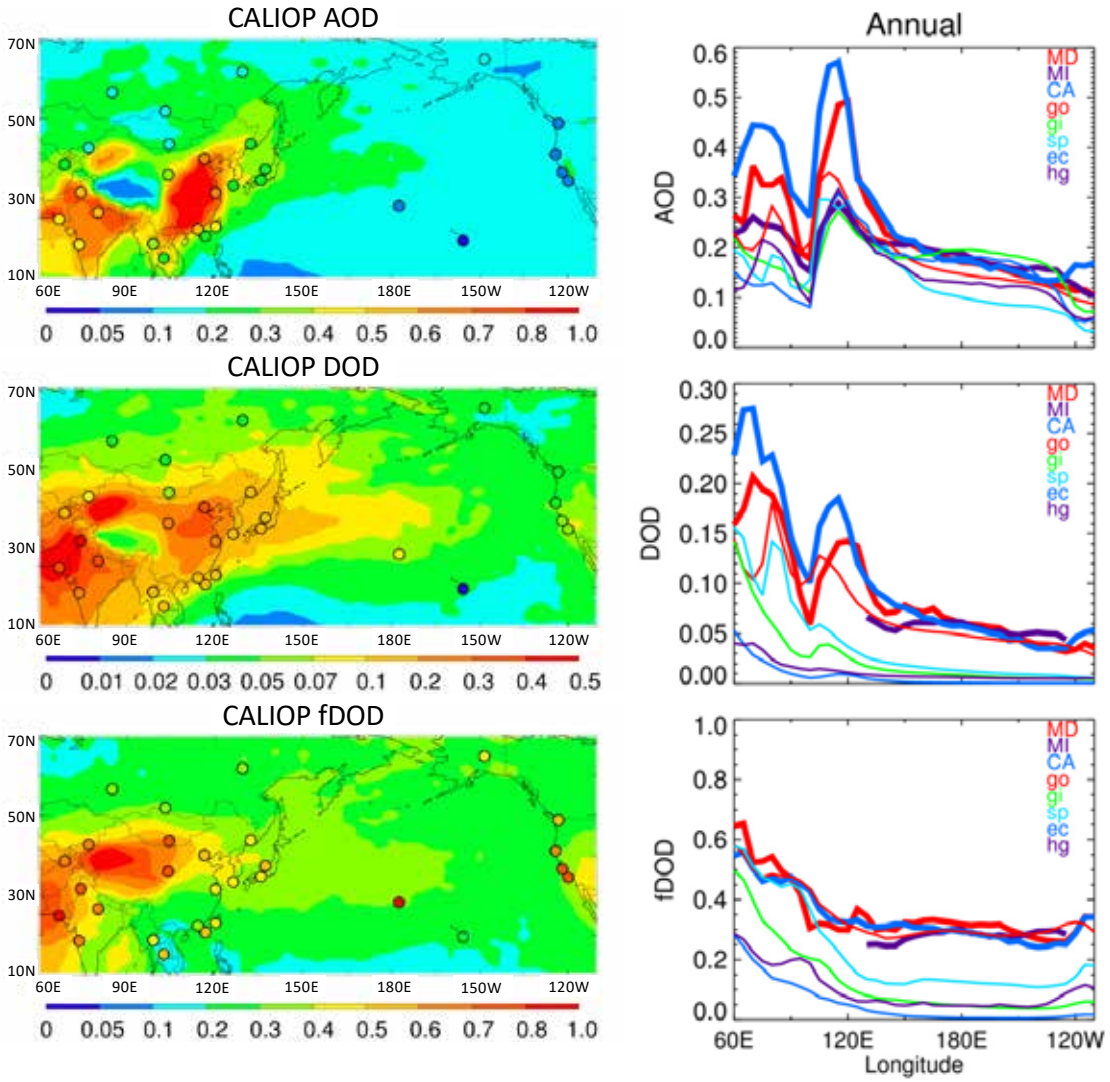

Figure 13. (left) Spatial distribution of mean AOD, DOD, and f_{DOD} from CALIOP averaged for 2007-2011, where, CALIOP excludes clear-air samples. Color circles superimposed on the map represent AERONET data. (right) same as Figure 4a except for CALIOP excludes clear-air samples.

Auxiliary Material for

Asian and trans-Pacific Dust: A multi-model and multi-remote sensing observation analysis

Dongchul Kim[1,2], Mian Chin[2], Hongbin Yu[2], Xiaohua Pan[2,3], Huisheng Bian[2,4], Qian Tan[5,6], Ralph A. Kahn[2], Kostas Tsigaridis[7,8], Susanne E. Bauer[7,8], Toshihiko Takemura[9], Luca Pozzoli[10], Nicolas Bellouin[11], and Michael Schulz[12]

[1]Universities Space Research Association, Columbia, Maryland, USA

[2]Earth Sciences Division, NASA Goddard Space Flight Center, Greenbelt, Maryland, USA

[3]Earth System Sciences Interdisciplinary Center, University of Maryland, College Park, Maryland, USA

[4]JCET/UMBC, Baltimore County, Baltimore, Maryland, USA

[5]Bay Area Environmental Research Institute, Moffett Field, California, USA

[6]NASA Ames Research Center, Moffett Field, California, USA

[7]NASA Goddard Institute for Space Studies, New York, New York, USA

[8]Center for Climate Systems Research, Columbia University, New York, New York, USA

[9]Research Institute for Applied Mechanics, Kyushu University, Fukuoka, Japan

[10]European Commission - Joint Research Center, Ispra, Italy

[11]Department of Meteorology, University of Reading, Reading, UK

[12]Norwegian Meteorological Institute, Oslo, Norway

Introduction

There are a supplement table and six supplement figures. File names and figure captions are presented.

1. Table_S1.docx: AERONET site name, longitude, and latitude.

2. Table_S2.docx: Mean emissions from the Taklimakan desert (75°E-90°E, 35°N-45°N), Gobi Desert (95°E-115°E, 40°N-50°N), and Thar desert (60°E-80°E, 20°N-40°N). SRC_{all} is the sum of TAKL, GOBI and THAR deserts; SRC_{TAGO} is the sum of TAKL, GOBI; Total is the entire domain (60°E-140°W, 20°N-60°N) and the values are taken from Figure 4.

3. Suppliment_Figirures.docx

Supplement Figure Captions

Figure S1. Number of data samples (ncount) in million for January 2007 - December 2011: (a) -100<CAD<-20 and include clear-air; (b) -100<CAD<-70 and include clear-air; (c) -100<CAD<-20 and exclude clear-air; (d) -100<CAD<-70 and exclude clear-air. (e) ncount (-100<CAD<-20, include clear-air) minus ncount (-100<CAD<-70, include clear-air), (f) ratio of exclude clear-air to include clear-air (-100<CAD<-70), (g) percent ratio of CAD<-20 to CAD<-70 (exclude clear-air).

Figure S2. Comparison of monthly mean AOD between AEROENT and other satellite data and model values over the study domain. Number of total data point is 474 between 2000 and 2005. R, B, and E are the correlation coefficient, mean bias, and root-mean-square-error, respectively. Mean bias is defined as the sum of the ratio of the modeled or satellite AOD to AERONET AOD.

Figure S3. Monthly mean AOD over Land-West (60°E-100°E), Land-East (100°E-140°E), Ocean-West (140°E-180°E), Ocean-East (180E°-140°W) domains from top to bottom. Latitudinal ranges are 20°N to 60°N. Left- and right-columns are from satellites and models, respectively. All model plots are averaged from 2000 to 2005. Vertical bars are the standard deviation of monthly mean values.

Figure S4. Same as Figure S3 except for DOD.

Figure S5. Same as Figure S3 except for f_{DOD}.

Figure S6. Monthly mean DOD for 2000-2005 over the Taklimakan desert.

Figure S7. Map of precipitation (mm day^{-1}) of each season from models averaged from 2000 to 2005.

Table S1. AERONET site name, longitude, and latitude.

Site Name	Longitude (°E)	Latitude (°N)
Issyk-Kul	76.98	42.62
Dushanbe	68.86	38.55
SACOL	104.14	35.95
Kanpur	80.23	26.51
Pimai	102.56	15.18
Dalanzadgad	104.42	43.58
Tomsk	85.05	56.48
Karachi	67.03	24.87
Lahore	74.33	31.54
Pune	73.81	18.54
Chiang_Mai_Met_Sta	98.97	18.77
Dongsha_Island	116.73	20.70
Hong_Kong_PolyU	114.18	22.30
Chen-Kung_Univ	120.22	23.00
Irkutsk	103.09	51.80
Yakutsk	129.37	61.66
Midway_Island	-177.38	28.21
Mauna_Loa	-155.58	19.54
Bonanza_Creek	-148.32	64.74
Trinidad_Head	-124.15	41.05
Saturn_Island	-123.13	48.78
UCSB	-119.85	34.42
Monterey	-121.86	36.59
Taihu	120.22	31.42
Beijing	116.38	39.98
Gosan_SNU	126.16	33.29
Osaka	135.59	34.65
Noto	137.14	37.33
Ussuriysk	132.16	43.70

Table S2. Mean emissions from the Taklimakan desert (75°E-90°E, 35°N-45°N), Gobi Desert (95°E-115°E, 40°N-50°N), and Thar desert (60°E-80°E, 20°N-40°N). SRC_{all} is the sum of TAKL, GOBI and THAR deserts; SRC_{TAGO} is the sum of TAKL, GOBI; Total is the entire domain (60°E-140°W, 20°N-60°N) and the values are taken from Figure 4.

Model	Emission (Tg yr^{-1})			Ratio		
	TAKL (TA)	GOBI (GO)	THAR (TH)	$\frac{SRC_{all}}{Total}$	$\frac{SRC_{TAGO}}{Total}$	$\frac{TAKL}{GOBI}$
GO	252.9	209.4	134.4	0.88	0.68	1.21
GI	30.6	51.0	49.5	0.66	0.41	0.60
SP	208.6	166.0	273.2	0.78	0.45	1.26
EC	1.4	24.7	7.1	0.43	0.34	0.06
HG	31.2	103.5	200.9	0.69	0.28	0.30
Mean	104.9	110.9	133.0	0.7	0.4	0.68
STD	116.5	77.2	108.5	0.2	0.2	0.54
DIV	111.0	69.6	81.6	24.4	35.9	78.30

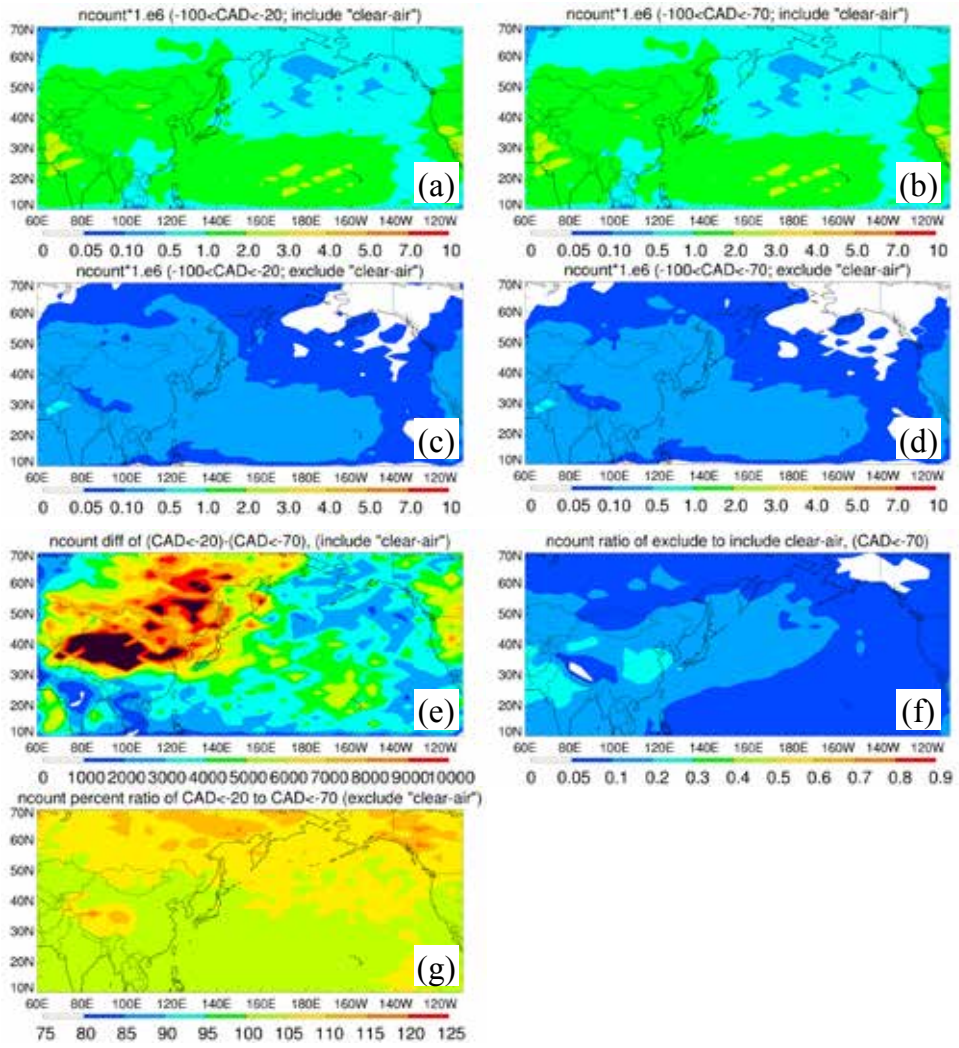

Figure S1. Number of data samples (ncount) in million for January 2007 - December 2011: (a) -100<CAD<-20 and include clear-air; (b) -100<CAD<-70 and include clear-air; (c) -100<CAD<-20 and exclude clear-air; (d) -100<CAD<-70 and exclude clear-air. (e) ncount (-100<CAD<-20, include clear-air) minus ncount (-100<CAD<-70, include clear-air), (f) ratio of exclude clear-air to include clear-air (-100<CAD<-70), (g) percent ratio of CAD<-20 to CAD<-70 (exclude clear-air).

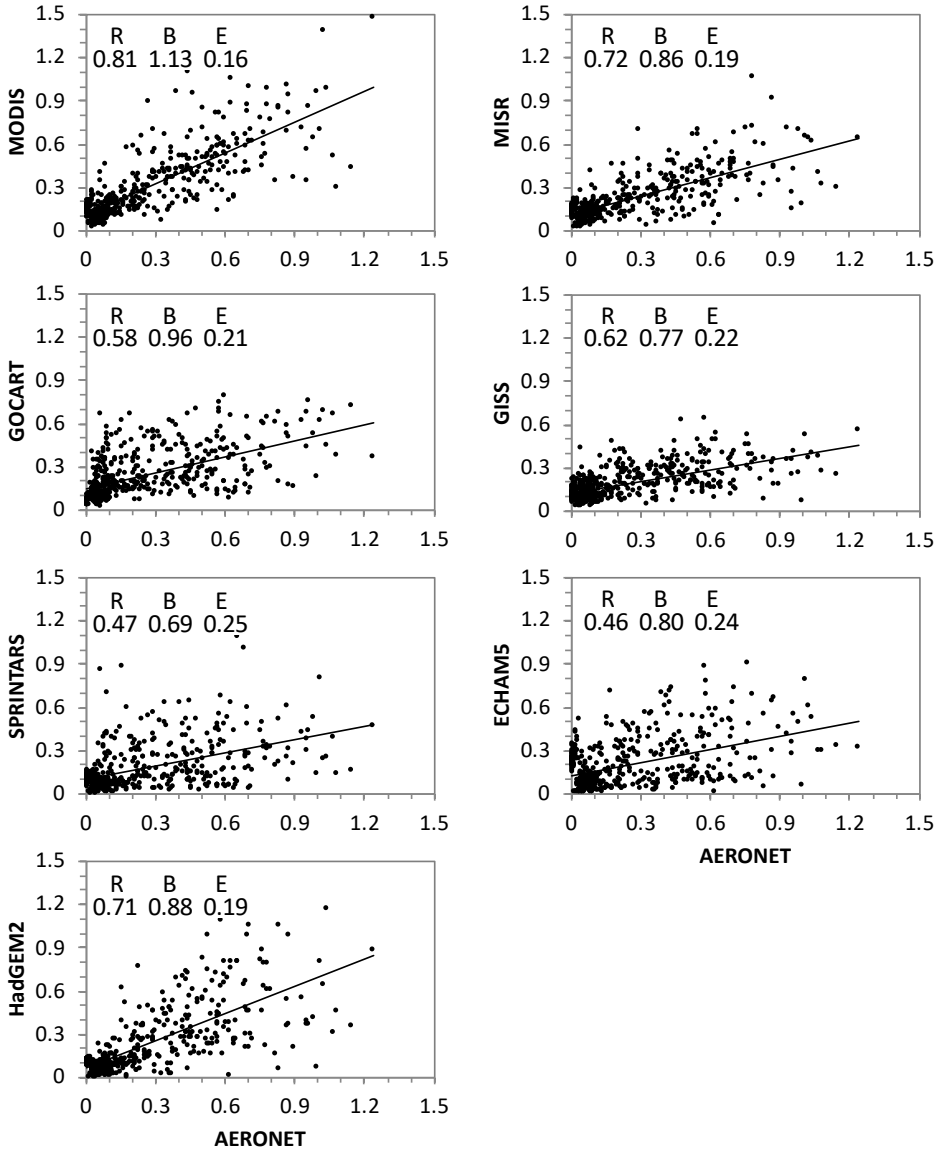

Figure S2. Comparison of monthly mean AOD between AEROENT and other satellite data and model values over the study domain. Number of total data point is 474 between 2000 and 2005. R, B, and E are the correlation coefficient, mean bias, and root-mean-square-error, respectively. Mean bias is defined as the sum of the ratio of the modeled or satellite AOD to AERONET AOD.

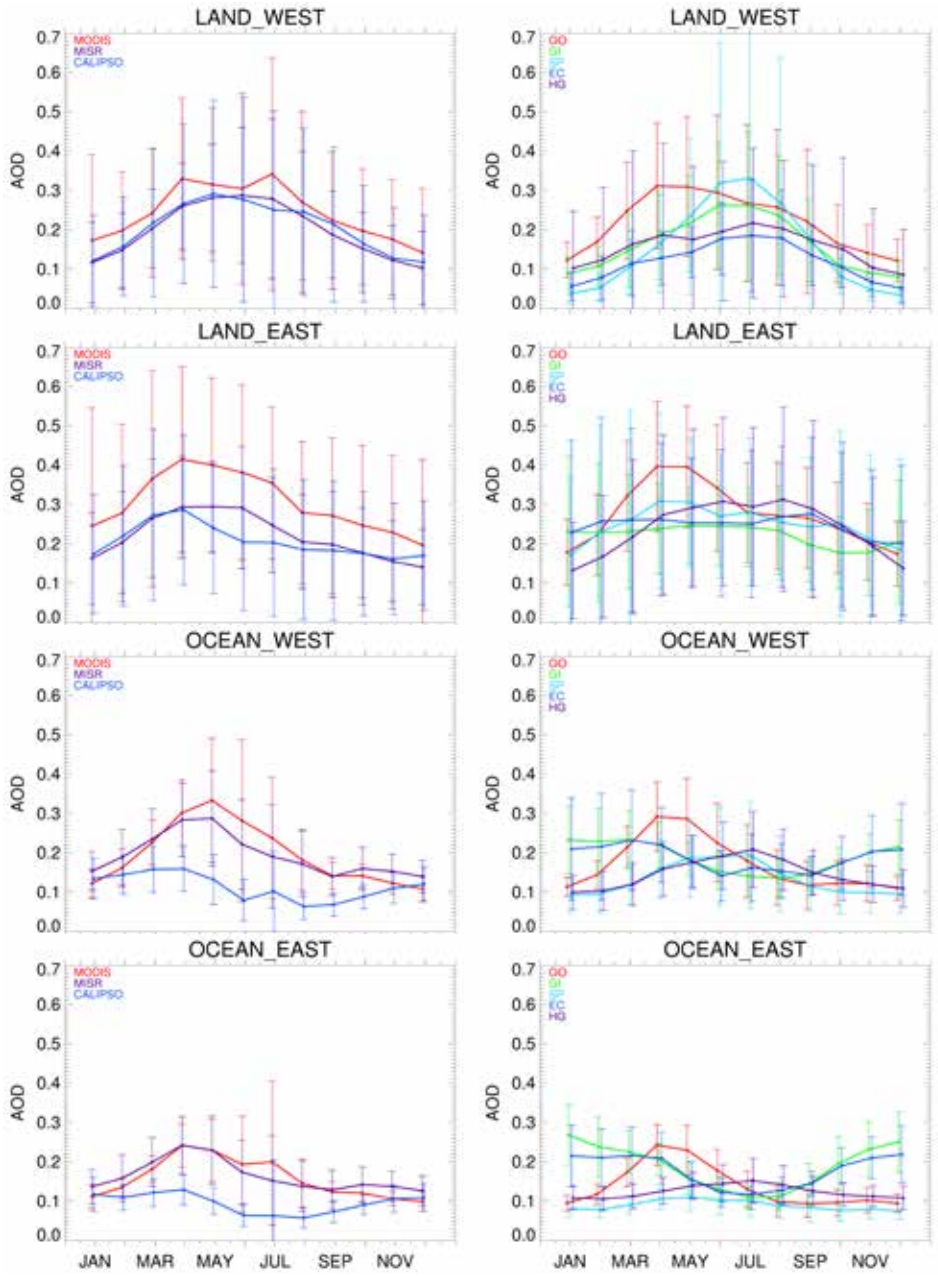

Figure S3. Monthly mean AOD over Land-West (60°E-100°E), Land-East (100°E-140°E), Ocean-West (140°E-180°E), Ocean-East (180E°-140°W) domains from top to bottom. Latitudinal ranges are 20°N to 60°N. Left- and right-columns are from satellites and models, respectively. All model plots are averaged from 2000 to 2005. Vertical bars are the standard deviation of monthly mean values.

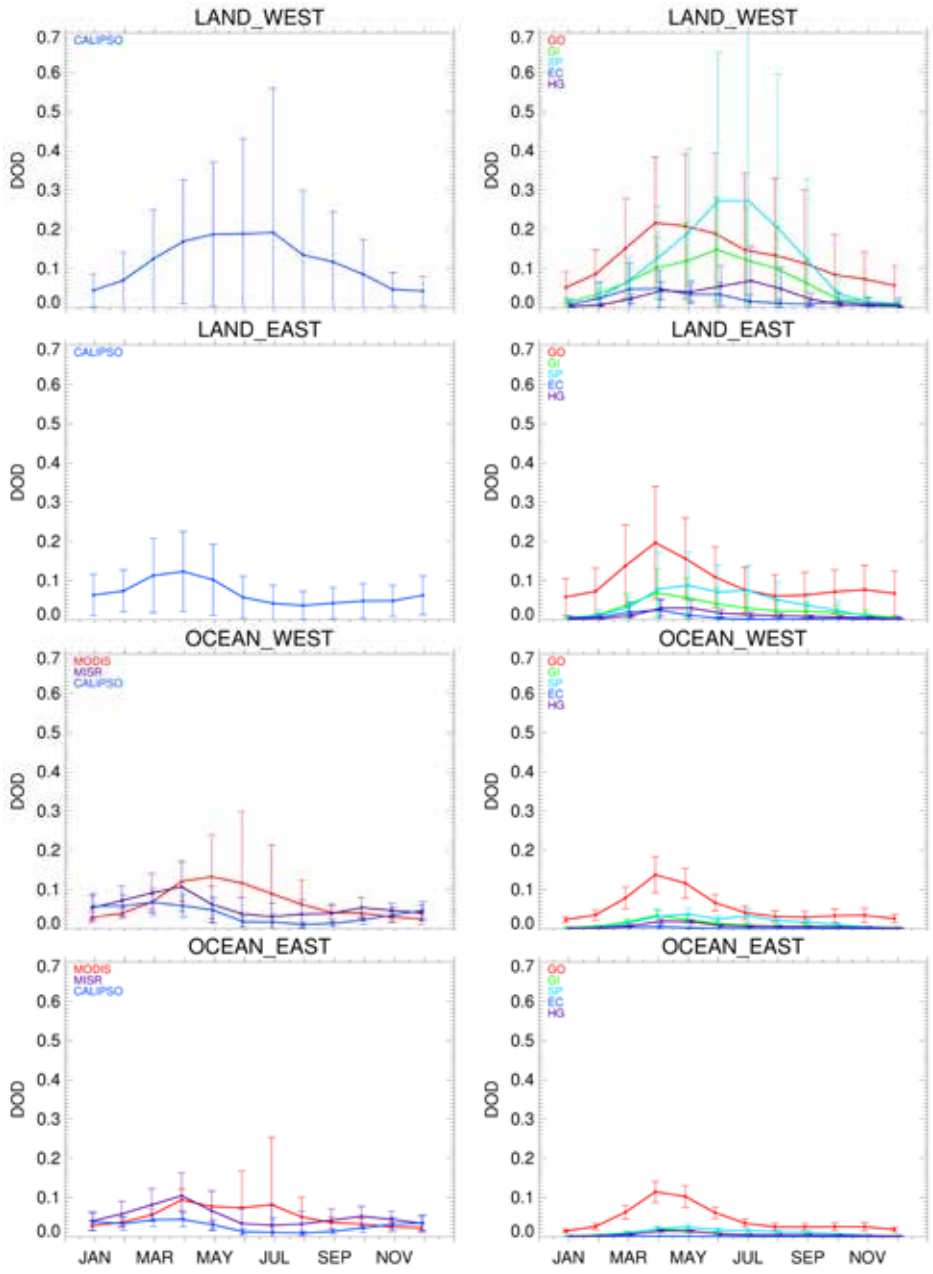

Figure S4. Same as Figure S3 except for DOD.

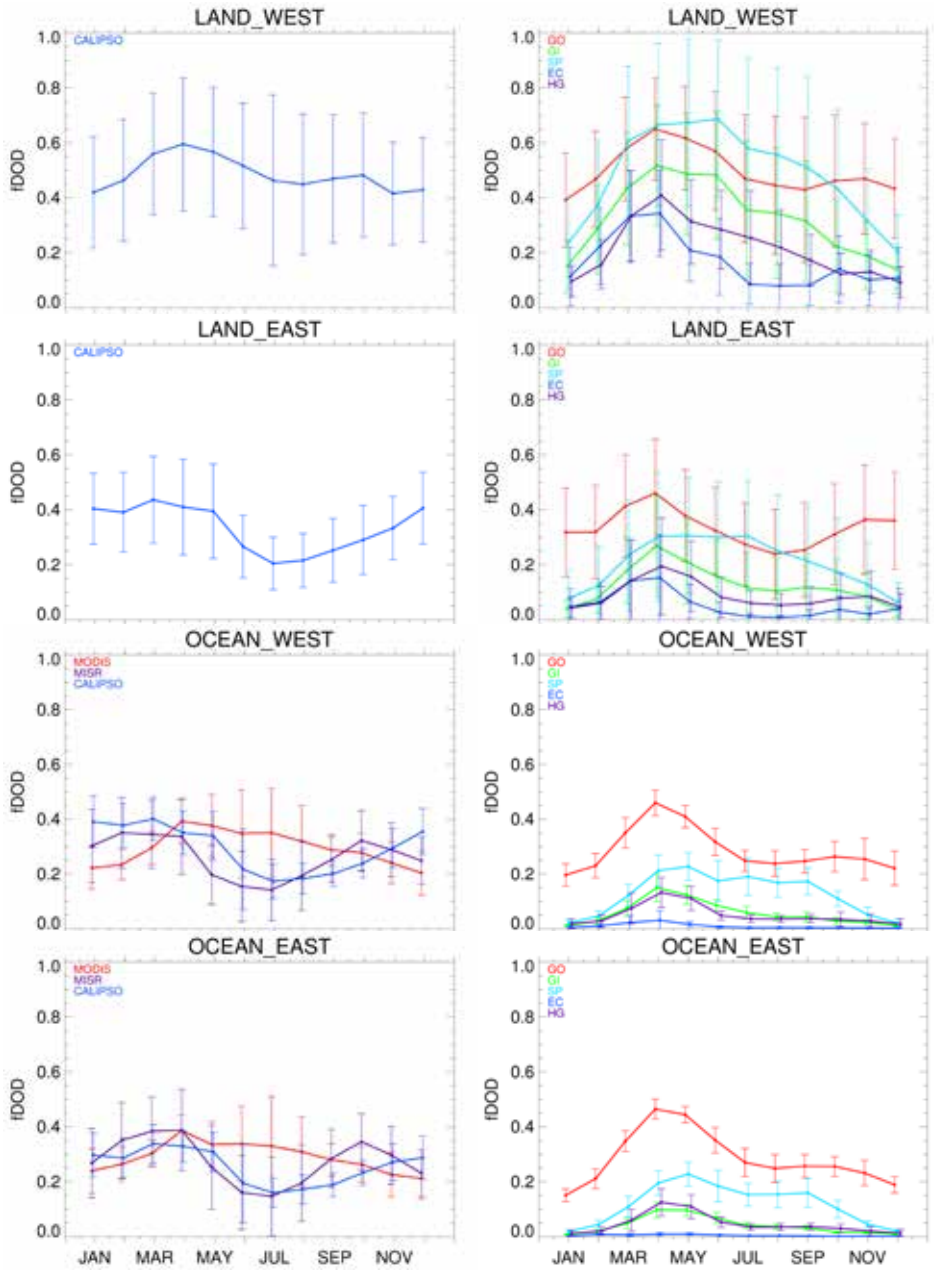

Figure S5. Same as Figure S3 except for f_{DOD}.

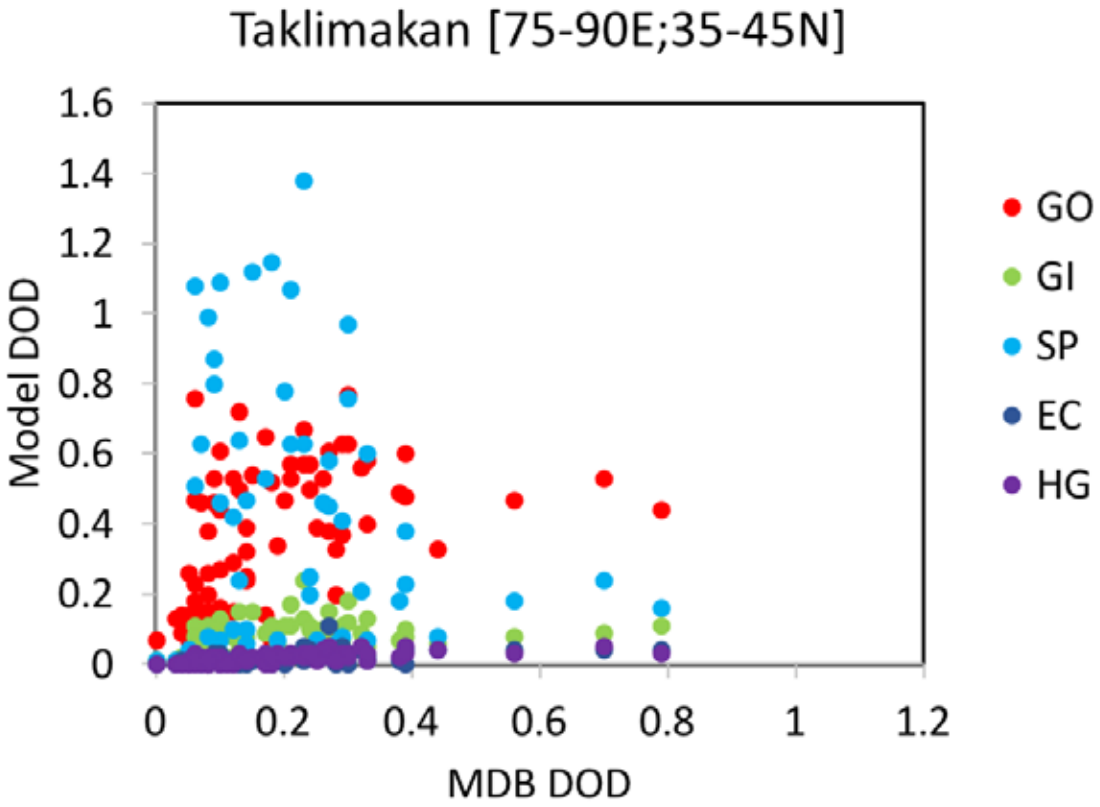

Figure S6. Monthly mean DOD for 2000-2005 over the Taklimakan desert.

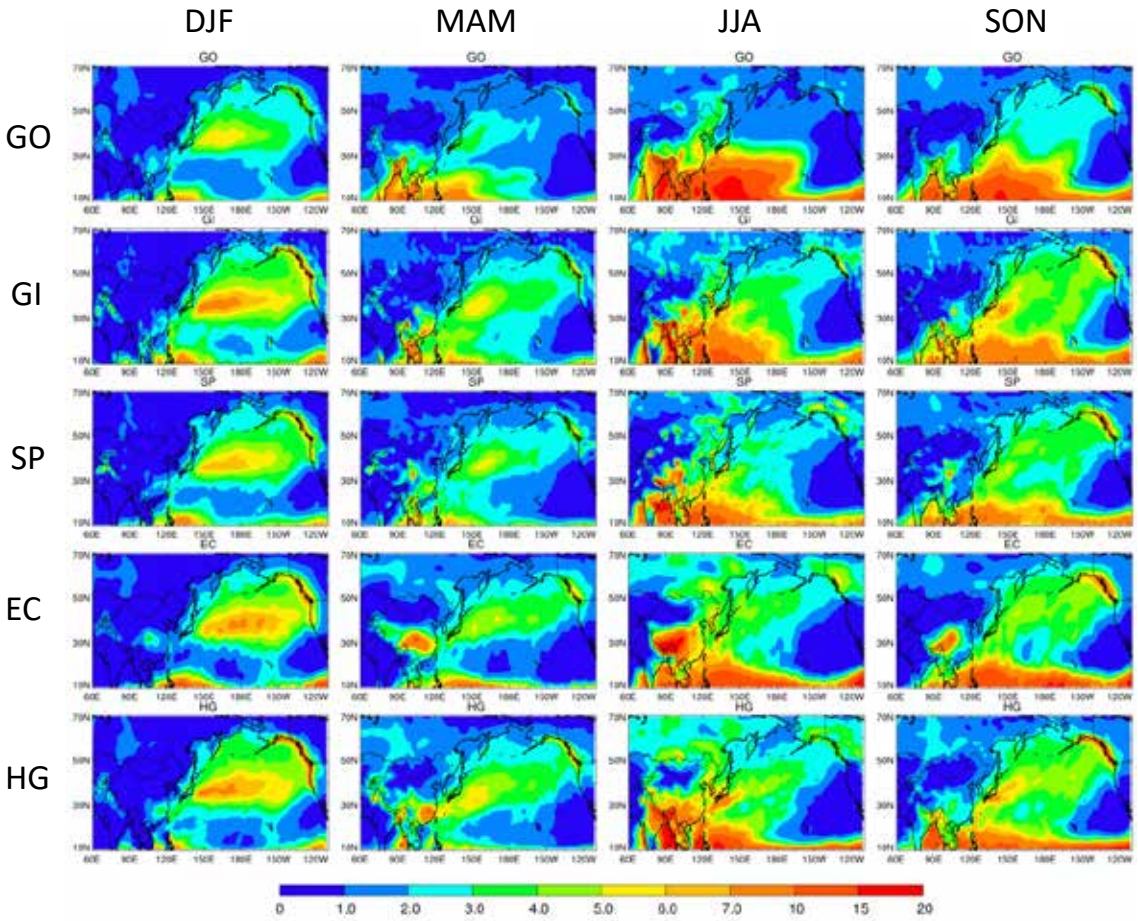

Figure S7. Map of precipitation (mm day^{-1}) of each season from models averaged from 2000 to 2005.